Comprehensive Assessment of A-Type Granite from South Sinai, Egypt: Geochemistry, Zircon Geochemistry, and Geochronology

Mohamed Abu Anbar[1], Mohamed F. Ghoneim[1], Tamer S. Abu-Alam[2,3], Dina Hamdy[1], YunPeng Dong[4], Bo Wang[5], Xiaoming Liu[4], Ahmed E. Masoud [1,6]

[1] Geology Department, Faculty of Science, Tanta University, 31527 Tanta, Egypt

[2] Arctic Sustainability Lab, Department of Arctic and Marine Biology, Faculty of Biosciences, Fisheries and Economics, UiT The Arctic University of Norway, 9037 Tromsø, Norway

[3] OSEAN-Outermost Regions Sustainable Ecosystem for Entrepreneurship and Innovation, University of Madeira Col´egio dos Jesuítas, 9000-039 Funchal, Madeira Island, Portugal

[4] State Key Laboratory of Continental Dynamics, Department of Geology, Northwest University, 710069 Xi'an, China

[5] State Key Laboratory for Mineral Deposits Research, School of Earth Sciences and Engineering, Nanjing University, 210023 Nanjing, China

[6] Nanjing Hongchuang Geological Exploration Technology Service Co., Ltd., 210046 Nanjing, China

*Corresponding author Dina Hamdy e-mail: dhamdy58@yahoo.com

Abstract: The A-type granites are an important component of the Earth's continental crust and play a significant role in understanding crustal evolution and tectonic processes. This study presents a comprehensive assessment of A-type granites from Ataitir El Dehami granites (ADG) that located at the north-western part of Wadi Seih area in South Sinai, using geochemistry, zircon geochemistry, and geochronology characteristics. The geochemical analysis reveals that ADG are characterized by high silica content, relatively high FeO*, and high alkali concentration consistent with the A-type granites that derived from the melting of tonalite sources. Zircons from Ataitir El Dehami granites have high REE contents with Ce enrichment and depletion of Eu, which, together with the high U/Yb ratios, suggest that the studied granites were generated from melting of continental crust rocks. Zircon U-Pb geochronological data indicates that the granite emplacement occurred around 575 to 603 Ma throughout continuous exhumation pulses. The isotopic analyses also indicate that the presence of inherited zircon grains (735± 9Ma). The present data suggest that the studied granites were formed in a post-collisional setting, and represent the transition stage from convergence to extension that occurred at 600 Ma.

Introduction

The Sinai Peninsula represents the most northerly segment of the Arabian–Nubian Shield (ANS) that is considered the best-exposed and largest Neoproterozoic juvenile continental crust on Earth (Stern, 2008; Johnson et al., 2011). The ANS is a major orogenic system that formed near the end of the Proterozoic as a result of the closure of the Mozambique Ocean and the collision between East and West Gondwana (Dilek and Ahmed 2003; Johnson and Woldehaimanot 2003; Abu-Alam et al. 2014).

Growth of the ANS crust occurred throughout most of the Neoproterozoic (900–580 Ma; Stern, 1994; Nehlig et al., 2002; Stern, 2008; Stern and Johnson, 2010) through three main stages, (1) accretion stage (870–670 Ma) comprising the formation and amalgamation of arc terrains onto East Gondwana continental block (Stern, 2002; Johnson et al., 2011; Peng et al., 2022); (2) collision stage (650–620 Ma) between the accreted juvenile ANS crust with the ancient pre-Neoproterozoic Saharan Metacraton (Stoeser and Frost, 2006; Abu Alam et al., 2014), and (3) post-collisional stage (620–580 Ma), initiated after the collision, and involved extensional collapse of the thickened lithosphere, inducing extension and thinning of the ANS crust (El-Bialy, 2010; Eyal et al., 2010).

Syn-orogenic calc-alkaline magmatism (650– 620 Ma), associated with the subduction phase of the north ANS, was followed by a subsequent phase of post-collisional magmatism, that produced high-K calc-alkaline and alkaline rocks (Jarrar et al., 2008; Moussa et al., 2008; Azer and El-Gharabawy, 2011). The post-collisional granitoid rocks of the north ANS, including those outcropping in the Sinai Peninsula of Egypt, provide significant information on these late magmatic phases and their contributions to the growth of the ANS continental crust.

Compared to other juvenile continental crusts, the ANS is characterized by widely distributed granitic plutons of different geochemical affinities that developed in varied tectonic settings. In Sinai, granitoids are more prevalent than any other region of the ANS, comprising nearly 70% of the total area of the Sinai basement (Bentor, 1985).

Two distinctive groups of granitoid rocks are identified in the ANS crystalline basement complex of Sinai: (1) Older Granites (860–610 Ma) including syn-tectonic, calc-alkaline I-type granitic masses (quartz diorite, tonalite to granodiorite) that were evolved in orogenic volcanic arc settings (Stern and Hedge, 1985; Hassan and Hashad, 1990; Stern, 1994; Moussa et al., 2008; Bea et al., 2009) and (2) Younger Granites (610–580 Ma) comprising highly fractionated calc-alkaline and alkaline A-type granites, and are believed to be emplaced throughout the post-collisional phase of the shield evolution (Beyth et al., 1994; Moussa et al., 2008; Ali et al., 2009; Eyal et al., 2010; Abdelfadil et al. 2018).

Although numerous studies on the granitic rocks of the Sinai Peninsula that have suggested a wide variety of geochemical characteristics and tectonic regimes (Moussa et al., 2008; Ali et al., 2009; Eyal et al., 2010), the origin of the post-collisional granitoid rocks (evolved by partial melting of lower/middle crustal materials or by fractionation of mantle-derived melts; Azer et al., 2019; El-Bialy et al., 2020) and geotectonic evolution are still controversial.

The present work focuses on the petrogenesis of late Neoproterozoic post-collision alkaline granites from southern Sinai (i.e., Ataitir El Dehami granites). We present new geochemical, geochronological, and zircon geochemical data for these granites. We use the new data in this contribution to evaluate genesis, tectonic setting and emplacement age of these granites.

Geological setting

In the southern Sinai Peninsula, the Precambrian basement is built up of four metamorphic complexes (namely, Zaghra, Kid, Feiran-Solaf, and Taba, Fig. 1a) that are separated by voluminous late- to post-tectonic unmetamorphosed granitoids, (e.g., Eyal et al., 2010; Be'eri-Shlevin et al., 2011; Abu-Alam and Stuwe, 2009). The study area (i.e., Ataitir El Dehami granites) is located at the northwestern part of Wadi Seih area (Fig. 1a) which represents the northwestern extension of the Feiran-Solaf complex. Wadi Seih area is composed of orthogneisses, paragneisses, migmatites, syn- and post-tectonic intrusions, and volcanics (Fig.1b).

Paragneisses are exposed in Wadi Tayeba and partly in Wadi Umm Agraf. They are buff and gray-colored, medium to coarse-grained (1–5 mm), and strongly foliated. Two essential varieties of paragneisses are observed, namely orthopyroxene-free paragneisses and orthopyroxene-bearing paragneisses with documented ages 1039-627Ma (Abu Anbar et al., 2023).

Orthogneisses are well exposed at Wadi Seih, Wadi Sidri, Wadi Umm Maghar, and Wadi Umm Agraf, and their area occupies about 180 km^2 (Fig. 1b). They are gray or pink in color, medium- to coarse-grained (2–5 mm) with moderate to high relief, and have a granitic composition. The outcrops are dissected by major faults trending NE-SW and are crosscut by a number of NE-SW-trending dykes of varying composition. The orthogneisses at Wadi Seih are intruded by Ataitir El Dehami granites and hornblende gabbros with documented ages 994-619Ma (Abu Anbar et al., 2023).

Migmatites occur in both paragneisses and orthogneisses. Migmatites formed in paragneisses occur along the contacts between paragneisses and granodiorite-tonalite associations. There are two types of migmatites observed in the orthogneisses; migmatites with a folding structure and migmatites with a ptygmatic folding structure (Abu Anbar et al., 2023).

Amphibolites occur as enclaves, bands and linear bodies of variable thickness in para- and orthogneisses as unmapped units. Depending on geochemical data and field observation, Abu Anbar et al. (2023) classified the amphibolites in Wadi Seih area into ortho- and para-amphibolites.

Hornblende gabbros are exposed mainly at Wadi Naba in the southwestern part of Wadi Seih area with documented age 617±19 Ma (Abu Anbar, 2009). (Fig. 1b). They are coarse-grained (up to 5 mm), dense, and grayish-colored. The gabbroic intrusion exhibits sharp intrusive contacts with the gneisses and sends offshoots and apophyses into them.

Granodiorite-tonalite associations are exposed at the extreme northeastern part of Wadi Seih and the southern part of the mapped area at Gabal Umm Radhim and Gabal Hallal (Fig. 1b). They are whitish-gray to dark-gray in color and coarse- to medium-grained (1–5 mm) with a massive appearance. They intrude into the hornblende gabbros (Fig. 1b).

Alkali-feldspar granites and syenogranites are located at the NW part of the mapped area (i.e., G. Ataitir El Dehami). The outcrop (~ 65 km^2) has high to moderate relief with medium- to coarse-grained rocks (2-5 mm) with a pinkish-white color (Fig. 2a). They intrude orthogneisses, migmatites (Fig. 2b and c), and hornblende gabbros with discordant sharp intrusion contact. The pluton is severely dissected by a group of dykes of different compositions including mafic types and less common felsic types trending NE-SW (parallel to the Gulf of Aqaba, Fig. 2d). The present work focuses on the alkali-feldspar granites and syenogranites of G. Ataitir El Dehami.

Petrography

G. Ataitir El Dehami granites are represented mainly by alkali-feldspar granites and rarely syenogranites. They are composed mainly of k-feldspar (80-65%) and quartz (20-30%), with a minor amount of plagioclase (10-20%) and biotite (5-10%). The most prevalent accessory minerals are zircon, iron oxides, and apatite, whereas chlorite and sericite are secondary minerals. They show perthitic and hypidiomorphic textures (Supplementary Fig. 1a).

Alkali feldspars (microcline and orthoclase) form euhedral to subhedral crystals (up to 1.2 mm in size, Supplementary Fig. 1a and b). Microcline occurs as subhedral crystals with crosshatched twinning (Supplementary Fig. 1b). Quartz forms anhedral to subhedral crystals up to 0.6 mm, filling the interstices between the feldspar crystals. Plagioclase is commonly albite and forms tabular crystals and occasionally intergrown with the K-feldspar forming perthitic texture. It is twinned according to the Albite and Carlsbad laws. Biotite forms small flakes and is partly altered into chlorite (Supplementary Fig. 1d). Muscovite is represented by a few subhedral crystals that show low relief and are sometimes associated with biotite in a subparallel arrangement (Fig. 3c). Sericite occurs as an altered product of k-feldspar.

Analytical techniques

Microprobe mineral analyses have been performed at the Department of Mineralogy and Petrology, Institute of Geological Sciences, Wroclaw University, Poland, using an electron microprobe (Cambrian Microscan Mg). The analytical conditions were carried out at 15 kV accelerating voltage, 50 nA beam current, and 15 s counting time. The chemical formulae are calculated using MinPet software (Richard, 1995) and listed in Table 1.

Representative rock samples from G. Ataitir El Dehami granites were analyzed for whole-rock major, trace, and rare earth elements by X-ray fluorescence spectrometry (XRF) on pressed powder pellets using an ARL Advant–XP spectrometer, following the full matrix correction method proposed by Lachance and Trail (1966**)**. Accuracy is generally lower than 2% for major oxides, whereas the detection limits for trace elements range from 1 to 2 ppm. Replicate analyses on trace elements gave a precision lower than 5%. All analyses were carried out in the laboratories of Ferrara University, Italy. Bulk-rock analysis data are listed in Table 2.

Zircon separated from five representative rock samples from G. Ataitir El Dehami granites were analyzed for U-Pb ages and geochemistry. Samples were first crushed using conventional crushing and then separated using heavy liquids and a magnetic separator. Zircons were handpicked from each sample, pasted on the resin disc under the binocular microscope, and then polished to expose the grain centers. Transmitted light, reflected light, and cathodoluminescence (CL) images were collected on a microscope and a JEOL scanning electron microscope.

Zircon U–Pb isotopic composition and trace element analyses were performed by Laser-ablation inductively coupled plasma mass spectrometry (LA-ICPMS). The analyses were carried out at the Laboratory of Continental Dynamics, Geology Department, Northwest University, China. A pulsed 193 nm ArF Excimer laser with 50 mJ energy at a repetition ratio of 10 Hz coupled to an Agilent 7500 quadrupole ICP-MS was used for ablation. The detailed analytical procedures follow Liu et al. (2007). The repetition rate was 10 Hz, and the spot sizes were 20 μm in diameter. ICP-MS measurements were carried out using peak jumping (1 point per peak) mode, and the dwell time for each isotope was set at 6 ms for Si, Ti, Nb, Ta, and REE, 15ms for ^{204}Pb, ^{206}Pb, ^{207}Pb, and ^{208}Pb, and 10ms for ^{232}Th and ^{238}U. Each spot analysis consisted of approximately 30s of background acquisition and 40s of sample data acquisition. Every five analyses on unknown samples, external standards zircon 91500 measurement and NIST610 were frequently analyzed during analytical session. The $^{207}Pb/^{206}Pb$, $^{206}Pb/^{238}U$, and $^{207}Pb/^{235}U$ ratios were corrected using 91500 as external standards and calculated using GLITTER4.0 program. Common Pb correction was applied using the method of Andersen (2002). The weighted mean U-Pb ages and Concordia plots were processed using ISOPLOT program (version 2.49) of Ludwig (2001).

Results

Mineral chemistry

The chemical formulae of the feldspar were computed on the basis of 8 oxygen atoms and are listed in Table 1. The feldspar of the alkali feldspar granites has an albite composition on the Or-Ab-An ternary diagram of Deer et al. (1978) with an XCa ranging from 0.013 to 0.082 (with an average of 0.040).

The results of electron microprobe (EMP) analyses of biotite minerals and their chemical formulae, which were calculated based on 22 oxygen atoms, are listed in Table 1. Biotite crystals are characterized by relatively low TiO_2 (< 3 wt.%), enriched FeO (up to 39 wt.%), and MgO-depleted (< 2 wt.%), leading to Fe# ratios between 0.92 and 0.94, which classified them as annite and siderophyllite (Rieder et al. 1998, Deer et al. 2013). This classification is confirmed by the chemical contents (i.e., Al, Fe^{3+}, Ti, Mg, Fe^{2+} and Mn) of the biotite which reveal that the studied biotites have a siderophyllite, Fe-biotite composition according to Foster, 1960.

The chemical formulae of the studied chlorite were calculated based on 14 oxygen atoms and are listed in Table 1. Chlorite of the studied granites has high FeO content with an average of 43.42 wt.% and low content of SiO_2 and MgO with an average of 25.19 wt.% and 1.73 wt.%; respectively. The studied chlorite is classified as pseudothuringite according to the nomenclature of Hey, 1954.

Whole rock geochemistry

Major and trace element compositions.

The concentrations of major and trace elements of the studied granites are listed in Table 2 as weight percent (wt.%) for major oxides and as parts per million (ppm) for the trace elements. On the basis of major elements, the analyzed samples of G. Ataitir El Dehami granites are silica-rich, with SiO_2 ranging from 73.91 to 75.96 wt.% and moderate Al_2O_3 ranging from (13.23–14.27 wt.%). They have high contents of alkalis, with Na_2O (3.77–4.47 wt.%), K_2O (4.63–5.05 wt.%), but low abundances in Fe_2O_3 (0.80–1.27 wt.%), MgO (0.06–0.19 wt.%), CaO (0.37–0.73 wt.%) and P_2O_5 (0.01–0.3%). The most variable trace elements are Ba (24–147 ppm), Sr (6–29 ppm), Rb (135–282 ppm), Zr (95–171 ppm), Nb (9–22 ppm), and Th (23–30 ppm). All samples have SiO_2 concentrations greater than 70% and are thus classified as highly evolved felsic rocks.

Petrochemical classification

Plotting granitic samples of G. Ataitir El Dehami on the total alkali-silica (TAS) classification diagram (Middlemost., 1994; Fig. 3a), the samples are plotted in the granite field. They are mainly alkali feldspar-granite, except sample SA11 straddles the field of alkali-feldspar granite and syenogranite on R1-R2 multicationic diagram (De la Roche et al., 1980; Fig. 3b). The alkalinity of the granitic samples was measured using K_2O vs SiO_2 diagram (Peccerillo and Taylor, 1976) and Maniar and Piccoli (1989) diagram. The granite samples with K_2O contents of 4.63–5.05 wt.% are plotted in the area of high-K calc-alkaline series (Fig. 3c). They show relatively weakly peraluminous character (Fig. 3d), with obvious low A/CNK values (molar $Al_2O_3/(CaO+Na_2O+K_2O)$ which range from (1 to 1.08). The Ataitir El Dehami granites with high differentiated indices (DI = sum of normative Q+ Or +Ab: Thornton and Tuttle, 1960), range from 93.57 to 96.51 plot in the field of differentiated calc-alkaline granites (Fig. 3e). Depend on the MALI index (Na_2O+K_2O-CaO) vs. SiO_2 diagram (Fig. 3f), all samples are mainly plotted in the alkali-calcic A-type field and are characterized by relatively high MALI values. Due to high FeOt/ (FeOt + MgO) ratios (0.86 to 0.99) all samples are plotted in the ferroan A-type field (Fig. 3g).

The present data are normalized to the primitive mantle (Sun and McDonough, 1989) (Fig. 3h). It is evident from the figure that the granites of Ataitir El Dehami are characterized by high concentrations of some large ion lithophile elements (especially Rb, Th, and Pb) and are relatively depleted in Ba, Sr, and some high field strength elements (HFSE; e.g., Ti and Nb). These geochemical characteristics are similar to crustal or arc magmatic rocks (Kelemen et al. 1990). The depletion in Ba, Sr and Ti elements, is probably attributed to extensive fractionation of apatite, plagioclase and Fe-Ti oxides (Brown et al., 1984), and the strong negative Nb anomaly may indicate that the parental magma had a crustal source (Barbarin, 1999).

Zircon U–Pb isotopes and trace elements

In order to study the genesis as well as constrain the crystallization events, 188 spots from five samples of G. Ataitir El Dehami granites have been analyzed for trace element contents and U–Pb isotopic concentrations. Zircons from these five samples were analyzed by LA-ICP-MS technique, aided by their Cathodoluminescence (CL) images. U–Pb analyses and their corresponding ages are presented in Table 3. The zircon trace element data are given in Supplementary Tables (S1-S5).

Sample SA12

Zircon grains from sample SA12 have an equant to partly round in habit of about 100-150 μm length and 70-120 μm width (Fig. 4a). In cathodoluminescence (CL) images, some zircon grains show relatively subhedral to euhedral rims with clear concentric oscillatory zoning, although a few zircons with high uranium contents are dark brown and turbid.

Twenty-five LA-ICP-MS analyses were conducted on fourteen single grains. The analyzed spots have U contents ranging from 196 to 2966 ppm, except for 3 spots of content (6338 ppm, 9523 ppm, and 18900 ppm). Th content is in the range 67-2285 ppm (except for 2 spots of content 6139 ppm and 11876 ppm) and Th//U ratios with an average of 0.46 (Supplementary Table S1) suggesting a magmatic genesis and crystallization from high SiO_2 magma (Kirkland et al., 2015). Zircon grains have variable niobium content (1.3- 766 ppm), hafnium varies from (5327-14150 ppm with an average of 9777 ppm) and U/Yb ratios with an average of 1.3. The U-Pb isotopic analyses yield a weighted mean $^{206}Pb/^{238}U$ age of 601±3.9 Ma, (±95% conf., MSWD = 0.46; Fig. 5a), which is interpreted as the crystallization age of this sample.

The chondrite-normalized zircon REE patterns (Fig. 6a) of the study sample indicate a rather steeply rising slope due to HREE enrichment relative to LREE. The individual HREE patterns of zircons from this sample are almost parallel with restricted ranges of high $[(Yb/Gd)_{CI} = 7.8–20.5]$, negative Eu anomalies $[(Eu/Eu^*)_{CI} = 0.01–0.11]$ and positive Ce anomalies $[(Ce/Ce^*)_{CI}$

= 0.72-17.4]. These features characterize typical REE patterns of unaltered magmatic zircons (Hoskin and Ireland, 2000; Belousova et al., 2002; Hoskin and Schaltegger, 2003; Grimes et al., 2015).

Sample SI82B

Zircons from sample SI82B exhibit different forms of equant to prismatic with subhedral rims and sizes of 80–250μm length and 50–100 μm width. The grains show homogenous textures. They partially display well-developed oscillatory zoning in CL images, indicative of magmatic origin (Hoskin and Schaltegger 2003; Yang et al., 2014). But other grains show only faint and broad zoning (Fig. 4b).

Forty-one LA-ICP-MS analyses were carried out for both cores and rims of twenty-nine zircon grains. The analyzed grains have variable U contents of (43-4990 ppm except for 8 spots from 5860 to 12103 ppm), Th (18-2766 ppm), and Th/U ratios of (0.3-0.72, most of the analyzed zircons have Th/U ratios ≥ of 0.5) (Supplementary Table S2) that could signify their magmatic origin (Kirkland et al., 2015). Zircon grains have Hf contents of (5905-15367 ppm), Nb (0.9–226 ppm except for 3 spots that have a very high value of content (604 ppm, 1386ppm, and 2003 ppm), and U/Yb ratios with an average of 1.64. The analyses yield a weighted mean $^{206}Pb/^{238}U$ age of 580±26 Ma (±95% conf., MSWD = 2.8) (Fig. 5b). This age is interpreted as the crystallization age of the dated sample.

CI-normalized zircon REE patterns (Anders and Grevesse, 1989; Fig. 6b) are similar to that of sample SA12, and are characterized by a negative slope from the middle [$(Yb/Gd)_{CI}$ = 2–22] due to serious HREE enrichment relative to LREE with distinctive positive Ce [$(Ce/Ce^*)_{CI}$ = 0.56 – 73], and negative Eu anomalies [$(Eu/Eu^*)_{CI}$ = 0.001–0.2], which is characteristic of unaltered magmatic zircons (Hoskin and Ireland, 2000). The cerium content in these zircons is relatively high, implying crystallization from an oxidized magma where tetravalent Ce was abundant (Hoskin and Schaltegger, 2003). The individual HREE patterns of zircons are almost parallel while the LREE segments exhibit somewhat dissimilar patterns as indicated by the wide variation in their $(Sm/La)_{CI}$ ratios (0.64-493).

Sample SA9

Zircon grains extracted from sample SA9 are well-developed euhedral equant to prismatic. These grains show sizes ranging from 120-320 μm in length and 50–100 μm in width.

Cathodoluminescence images (Fig. 4c) show that the zircons of this sample display more complex internal structures with well-developed oscillatory zoning evident in other crystals with multiple stages of zircon crystallization and its primary magmatic origin (Corfu et al., 2003; Barth and Wooden, 2010). The isotopic analyses yield a coherent Concordia age of 596±2.2 Ma (±95% conf., MSWD = 1.4, Fig. 5c), which is interpreted as the crystallization age of this sample.

A total of forty-one analyses were conducted on twenty-eight zircon grains. The analyzed spots have relatively high U contents of (76–9520 ppm except for one spot, which records U contents of 23409 ppm). Th content of (31–5359 ppm except for two spots that record 7077 ppm and 10609 ppm), and Th/U ratios of (0.25-1.17, with an average of 0.47) (Supplementary Table S3). These zircon grains yielded a wide range of Hf contents (6518-21685ppm), and U/Yb ratios with an average of 2.42.

The chondrite-normalized zircon REE patterns (Fig. 6c) show variations in middle to heavy REE negative slopes [(Yb/Gd)CI = 6.2-26.7], negative Eu anomalies [(Eu/Eu*)CI = 0.001-0.29 with average 0.027] and positive Ce anomalies [(Ce/Ce*)CI = 0.83 – 159.1]. These patterns are typical of unaltered magmatic zircons (Belousova et al., 2002; Grimes et al., 2015).

Sample SA11

Zircon grains extracted from sample SA11 are mostly prismatic to equant and sometimes rounded. They have regular rims with lengths ranging from 120 to 250 μm. In CL images, zircon grains are commonly homogenous and show oscillatory zoning, however, some grains show unzoned homogenous cores (Fig. 4d). Most of the zircons have systematic growth zoning from core to rim. Luminescent outer rims are rare, suggesting a general lack of metamorphic overgrowth.

A total of fourteen U-Pb LA-ICP-MS analyses were conducted on 28 zircon grains. These analyses have U contents of (126-6827 ppm (except for 2 spots which have content of 11537 ppm and 26.687 ppm), Th of 45-2820 ppm (except for 5 spots of 3551 ppm to 7734 ppm). Th/U ratios of (0.25-0.85) (Supplementary Table S4) favoring a magmatic origin of zircon crystals. The present zircon grains have Hf contents of (7051–15909 ppm), Nb contents of (1.44–201 ppm (except for 10 spots of 807–6420 ppm), and U/Yb ratios of (0.46 – 3.68). U-Pb isotopic analyses yield a weighted mean $^{206}Pb/^{238}U$ age of 603±15 Ma (±95% conf., MSWD = 3.3), (Fig. 5d), which is interpreted as the time of magmatic crystallization of this sample.

All zircons have REE patterns with negative slopes from the middle to heavy REE [$(Yb/Gd)_{CI}$ = 3.8-17.7] and have high negative Eu anomalies [$(Eu/Eu^*)_{CI}$ = 0.01–0.1 with average 0.05], and positive Ce anomalies [$(Ce/Ce^*)_{CI}$ = 0.85–42.56], (Fig. 6d).

Sample SI81C

Zircons separated from this sample are mostly euhedral to subhedral, stubby prismatic to equant with sizes ranging from 100 to 250 µm length and 50 to 100 µm width. CL images show that zircons of this sample display more complex internal structures with well-developed oscillatory zoning evident in other crystals with multiple stages of zircon crystallization and its primary magmatic origin (Corfu et al., 2003; Cavosie et al., 2006; Barth and Wooden, 2010) (Fig. 4e).

Forty-one LA-ICP-MS analyses were conducted on 39 grains from sample SI81C. The analyzed spots have a higher content of U (4924 – 24166 ppm) than the other samples except four spots, which record low U content range from 95-403 ppm. Th contents are range from 2127to 19519 ppm, except for four spots, which record low Th contents range from 71 to 580 ppm, as well as Th/U ratios range from 0.15 to 1.8, except for one spot records Th/U ratio of 5.88 (Supplementary Table S5). All zircon grains are presumed to be magmatic and crystallized from high SiO_2 magma (Corfu et al., 2003; Kirkland et al., 2015). These zircon grains have high Hf contents of (8468-14510 ppm (except for one spot that records 76 ppm) suggesting their crystallization at a higher degree of magmatic evolution (Hoskin and Schaltegger, 2003), Nb contents of (141-3500 ppm), and U/Yb ratios of (0.3–4.68).

The U-Pb isotopic analyses define two clusters of concordant dates, the younger cluster yields a mean concordant age of 575± 7.1 Ma, whereas the oldest cluster yields a Concordia age of 735± 9Ma, which implies, most probably inherited zircon related to the age of old crustal rocks protolith (Fig. 5e). Zircons from this sample show a constrained range of small Eu/Eu* values (0.001 – 0.9, average = 0.05) leading to seriously deep negative anomalies and positive Ce anomalies $(Ce/Ce^*)_{CI}$ = 0.9–148.96 (Fig. 6e).

The chondrite normalized trace element spider diagrams (Supplementary Fig.3) show that all zircons of the different granitic samples are characterized by enrichment in large ion lithophile elements of Th, U, Hf and have negative anomaly of Ti, La and Nb.

In general, The chondrite-normalized REE patterns (Fig. 6) of all zircon grains in the present study are characterized by a rather steeply rising slope due to serious HREE enrichment relative to LREE with distinctive positive Ce [(Ce/Ce*) range from 0.56 to 159.16] and negative Eu anomalies [(Eu/Eu*) range from 0.001 to 0.9], which is typical of unaltered magmatic zircons (Hoskin and Ireland, 2000; Hoskin and Schaltegger, 2003; Rubatto, 2017). Furthermore, all zircon grains of different samples exhibit roughly similar REE patterns (Fig.6) and similar CI-normalized trace element spider diagrams (Supplementary Fig. 3) with little change in total concentrations, which is evidence of their identical crystallization environments (Cao et al., 2011; Deng et al., 2019). Hoskin and Schaltegger, 2003 suggested that the negative Eu anomaly is attributed to plagioclase fractionation, whereas the positive Ce anomaly is associated with oxidation processes or an oxidizing environment. REE patterns of zircons separated from the studied samples show patterns similar to those of A-type granites (Zhao et al., 2018).

Discussion

Petrogenesis of granites

Genetic type: highly fractionated I-type or A-type?

Granites are classified as M-, A-, S-, and I-types (Whalen et al., 1987; Eby, 1990; Chappell et al., 2012). The production of M-type granites is mostly based on the differentiation of mantle-based magma with mantle-origin features (Dong et al., 2019). Because Ataitir El Dehami granites have a high concentration of SiO_2 and low MgO, they cannot be M-type granites. The S-type granites are featured by high aluminum saturation index (ASI) values (normally >1.1), and enriched isotopes with the appearance of garnet and/or cordierite (Bonin, 2007), due to the lack of these features, the studied granites cannot be S-type granite.

Sodium amphibole, aegirine, iron olivine, and other signature alkaline dark minerals are historically thought to be the most common indicators and distinctive features of A-type granites (Chappell, 1999; Wu et al., 2007; Li et al., 2018). Since Ataitir El Dehami granite lacks these minerals, so the most objective criterion for identifying I- and A-type granite is their chemical composition. Aluminous A-type granites with relatively higher SiO_2 contents can distinguish from I-type by their high (Na_2O+K_2O), FeOt/(FeOt + MgO) ratios, as well as HFSE, Ga, Zn, but low Ca, Ni, Cr, Sr, and Ba contents (Collins et al., 1982, Whalen et al., 1987, Bonin, 2007).

The granite samples from Ataitir El Dehami are characterized by slightly higher alkali contents [(Na_2O+K_2O) = (8.82 to 9.37)], display high FeOt/(FeOt + MgO) ratios (0.86 to 0.99) and are mostly plotted into the field of ferroan A-type granitoids (Fig. 3g, defined by 175 A-type granites worldwide; Frost et al., 2001). In addition, the studied granites belong to the high

K series (Fig. 3c). In the primitive mantle normalized trace element diagram (Fig. 3h) granite samples exhibit evident negative Ba, Sr, P, and Ti anomalies and high large ion lithophile elements (LILE) abundances, including Rb, Th as well as enrichment in some high field strength elements (HFSEs; e.g., Ga, Zn). They are also plotted into the field of within plate granites (Fig. 7f and Supplementary Fig. 2a) All these features are suggestive of an affinity to A-type granite.

In the discrimination diagrams of Na_2O vs. K_2O and Na_2O + K_2O/CaO vs. 10*^{4} Ga/Al (Fig. 7a and b; Collins et al., 1982 and Whalen et al., 1987, respectively), the studied samples plotted in the A-type granite field.

Even though granite samples from Ataitir El Dehami share many geochemical characteristics with A-type granites, they also exhibit some unique features. Firstly, the concentrations of Zr (95-171 ppm) and Zr + Nb + Ce + Y (171–339 ppm) are clearly lower than the lower limit of the typical characteristic of A-type granite (Zr = 250 ppm; Zr + Nb + Ce + Y = 350 ppm). These features suggest that the granite developed from highly fractionated granitic magmas (Whalen et al., 1987; Chappell, and White, 1992; Foley and Barth, 2000; Clemens, 2003).

Secondly, A-type granite has significant geothermal gradient and high-temperature features that significantly exceed those of other forms of granite. Owing to their lower Zr contents, the Ataitir El Dehami granites yield a narrow range of significantly lower zircon saturation temperatures (T_{Zr}) ranging between 761 °C and 826 °C (av. 786 °C). These whole-rock zircon crystallization temperatures are modest relative to those determined for other younger granites elsewhere in the Egyptian Nubian Shield (Moreno et al., 2014; El-Bialy and Omar, 2015; Sami et al., 2017; Abd El Ghaffar and Ramadan, 2018). The considerably low zircon saturation temperatures of the studied granites together with their low Zr contents imply derivation through low-temperature crustal fusion, which causes incomplete dissolution of the more refractory zircon. The above finding which is further supported by plotting these samples on Whalen et al., 1987, in the Na_2O + K_2O/CaO vs. (Zr + Nb+ Ce+ Y); discrimination diagram (Fig. 7c), reveals that the studied granites straddle the field of highly fractionated I- and A-type granite.

It is worth mentioning that the highly fractionated felsic I-type granites might show Ga/Al ratios and some major and trace element values that overlap those of typical A-type granites (Whalen et al., 1987). Hence, it is possible that the A-type characteristics of the studied rocks could be explained by extensive fractionation from I-type (tonalite) melt (Laurent et al., 2014; Fig. 7e).

This is further supported by alkalinity index of Sylvester's (1989), which classify the examined granitoids as highly fractionated calc-alkaline rocks based on the diagram of (Al_2O_3 + CaO)/ (FeO* + Na_2O+K_2O) vs. 100(MgO + FeO* + TiO_2)/SiO_2; Fig 4e). Furthermore, a single-stage partial melting would not provide granites with extremely low Sr (less than 100 ppm; 6-29 ppm) and high Rb concentrations (135–200 ppm), implying that Ataitir El Dehami granites may undergo intense fractional crystallization (Halliday et al., 1991; Farahat et al., 2011; Sami et al., 2018).

In terms of the trace elements in zircon, they are enriched in Pb, Th, U, and Hf elements and obviously depleted in Ti element, Ce shows a positive anomaly, and Eu shows a negative anomaly (Fig. 6), all of which also show the geochemical characteristics of A-type granite (Zhao et al., 2018).

Eby (1992) divided A-type granite into two subtypes (A1 and A2) with different origins and tectonic settings. The studied granites plotted within the A2 field (Fig. 7d). The A2-type granitoids represent magmas sourced from the underplated crust or continental crust that has experienced a cycle of island-arc magmatism or continent-continent collision.

Origin of A-type granites

The origin of the A-type granites is controversial and the subject of debate (Eby, 1990; Eby, 1992; Huang et al., 2011; Collins et al., 2021). Petrogenetic models proposed for their formation are (1) high crystallization differentiation of mantle-derived basaltic magma (Beyth et al., 1994; Ewart et al., 2004; Konopelko, et al., 2007); (2) mixing of mantle-derived and crustal materials (Clemens et al., 1986; Yang et al., 2006); (3) Partial melting of lower crustal material which include partial melting of granulite facies remnants after granitic magma extraction (Collins et al., 1982; King et al., 1997), and partial melting of calc-alkaline tonalite-granodiorite (Anderson and Bende, 1989; Farahat et al. 2007).

Ataitir El Dehami granites show depletion in Al_2O_3, CaO, MgO, Fe_2O_3, TiO_2, P_2O_5, Sr and Ba (Table. 2). Suggesting their evolution by extensive fractional crystallization from a less fractionated magma as suggested by many authors (e.g., Stern and Gottfried, 1986; Turner et al., 1992; Moghazi, 2002). Yet, the evolution of these rocks by a simple fractional crystallization process of a mantle-derived mafic magma and magma mixing is hampered by the absence of large volumes of contemporaneous mafic rocks, as would be expected if extensive fractional crystallization took place, and supported also by the absence of microgranular enclaves in the present granites. Furthermore, according to Eby (1992), Y/Nb ratios are essential for determining the parent source. Whereas magmas with Y/Nb ratios > 1.2 are indicative of crustal melts and those with Y/Nb values <1.2 are typical of melts generated from the mantle. As a result, the analyzed samples had Y/Nb ratios greater than 1.2 (Table 2), implying a crustal protolith for the granites under study. As well as the geochemistry of zircon supported this conclusion as the studied zircons are continental (Fig. 9e). Accordingly, we favor the derivation of Ataitir El Dehami A-type granites from the direct partial melting of middle to lower crustal rocks, followed by some differentiation.

It has been proposed that A-type granites originated from the partial melting of LILE-depleted granulitic residue in the lower crust, from which the granitoids melt were previously extracted (Clemens et al., 1986; King et al., 1997). In addition, the residual granulite facies in the lower crust are characterized by low K, Si and high in Ca, Al, and Mg (Anderson and Bender, 1989). However, the geochemical characteristics of the Ataitir El Dehami granites contrast sharply with this model.

In this study, a more accurate model for A-type granites was suggested to be the partial melting of underplated I-type tonalitic to granodioritic source (Creaser et al., 1991). On the Al_2O_3/(FeOt + MgO)–CaO–5(K_2O/Na_2O) ternary diagram of Laurent et al., 2014 (Fig.7e), the samples of Ataitir El Dehami granites share similarities with magmas derived from the melting of tonalite sources which most probably derived from crustal rocks (King et al., 1997).

Tectonic setting

In order to determine the tectonic setting of the studied granites, the tectonic discrimination diagrams for granitic rocks of Pearce et al. (1984) are used (e.g., Fig.7f). These discrimination diagrams subdivide the granites into four main groups according to the tectonic setting: 1) Oceanic Ridge Granites (ORG), 2) Volcanic Arc Granites (VAG), which are produced from volcanic arc magmatism and mainly calc-alkaline, 3) Within Plate Granites (WPG), which associate alkaline and peralkaline magmas in anorogenic suites, and 4) Collision Granites(COLG), which are usually peraluminous granites that result from anatexis of sedimentary rocks during the continent collision.

According to Nb versus Y diagram, samples are generally plotted in the within-plate granite (WPG) field except sample SA9 plotted in the volcanic arc field (Fig. 7f). However, the tectonic setting of the studied granites falling at the intersection of within plate granites (WPG), arc granites (VAG) and syn-collisional granites (syn-COLG). Therefore, the granitic rocks under investigation are still controversial, and perhaps falling samples in this intersecting field could be accepted as a post-collisional granite (post- COLG) field (Pearce, 1996). Accordingly, the Ataitir El Dehami granites can be clearly classified as post collisional granites (Supplementary Fig. 3a and 3b; Pearce, 1996; Maniar and Piccoli, 1989, respectively).

Geochemistry of zircon

Magmatic versus hydrothermal zircon type

Zircons are commonly formed through the crystallization of magma, but they can also form from hydrothermal and metamorphic fluids (El-Bialy and Ali, 2013; Sheng et al., 2012; Sakyi et al., 2019). It has been proposed that zircons originating from magmatic processes generally exhibit identical REE patterns (Hoskin, 2005; Xia et al., 2010), while those derived from other processes can be distinguished by their own REE patterns (Hoskin and Schaltegger, 2003; Wang et al., 2012).

For instance, the presence of LREE enrichment in zircon is often associated with hydrothermal processes, and therefore, hydrothermal zircons display lower (Sm_N/La_N) and smaller Ce anomalies (Ce/Ce*) compared to magmatic zircons (Hoskin, 2005). However, several studies have indicated that some magmatic zircons may not differ from hydrothermal zircons in terms of chemical composition (Fu et al., 2009; Schaltegger, 2007).

Zircon grains in the present study are characterized by a rather steeply high slope due to serious HREE enrichment relative to LREE with distinctive positive Ce [(Ce/Ce*) range from 0.56 to 159.16] and negative Eu anomalies [(Eu/Eu*) range from 0.001 to 0.9], which is typical of unaltered magmatic zircons (Hoskin and Ireland, 2000; Hoskin and Schaltegger, 2003; Rubatto, 2017).

Hoskin and Schaltegger (2003) hypothesized that the Th/U ratio can be used as a reliable indicator for identifying the origin of zircon. Hydrothermal zircons typically exhibit Th/U ratios ranging from 0.1 (e.g., Hoskin and Schaltegger, 2003) to 0.3 (e.g., Hu et al., 2012), whereas Th/U ratios for magmatic zircons have been proposed to be ranging from 0.32 to 0.7 (e.g., Rubatto, 2002; Hoskin and Schaltegger, 2003; Fu et al., 2009; Li et al., 2014). Zircons from the studied granites displayed Th/U ratios of 0.45–0.69 with only a few zircon grains with Th/U ratios lower than 0.3. This suggests that most zircons are magmatic origin, while some zircon grains exhibit hydrothermal origin.

Moreover, zircon crystallization temperature can also serve as a method of distinguishing between hydrothermal zircons, which usually crystallize at temperatures below 500°C, and igneous zircons, which crystallize at temperatures above 500°C (Fu et al., 2009). The estimated temperature of zircon crystallization obtained from Ti-in-zircon thermometry exceeds 500°C, (average $T_{Ti\text{-}in\text{-}zrc}$ = 728 °C), indicating a magmatic origin.

Furthermore, Li et al. (2014) have demonstrated that zircons derived from different sources display diverse internal structures, growth morphology, and sizes. For instance, in cathodoluminescence (CL) images (Fig. 4), zircons of magmatic origin commonly exhibit distinct internal zoning, while hydrothermal zircons possess weak or absent zoning. The majority of zircons found in Ataitir El Dehami granitoids display regular concentric zoning patterns, which are characteristic of magmatic zircons.

Oxidation conditions of the magma

Zircon REE compositions can be applied as a proxy for constraining the magma properties of granitic intrusions, specifically the magma's oxidation state (Trail et al., 2012; Burnham and Berry, 2012; Lu et al., 2016). The magnitude of cerium and Eu anomalies have been commonly utilized to reflect the redox conditions of magmas, as an increase in the oxidation state of magma enhances the positive Ce anomaly but weakens the negative Eu anomaly in zircon (Shen et al., 2015). Thus, zircon Eu anomaly (Eu/Eu*) and Ce anomaly (Ce/Ce*) can be used to reflect the oxidation states of parental magma (Dilles et al., 2015; Loader et al., 2017). Following the calculation method of Loader et al. (2017), the calculated Ce/Ce* values from Ataitir El Dehami granites are high and vary widely between 0.56 and 159 with an average of 12.6, whereas the Eu/Eu* values (Hoskin and Schaltegger, 2003) of these samples are variable and range between 0.001 to 0.9 with an average of 0.05.

A plot of Ce/Ce^* vs. Eu/Eu^* (Fig. 8a) is very useful to infer the oxidation conditions during the crystallization of the magma. A positive linear to curvilinear correlation between Ce and Eu anomalies would be expected if both anomalies were simply controlled by the oxidation condition during zircon crystallization (Cao et al., 2011; Orejana et al., 2011; El-Bialy and Ali, 2013; Wang et al., 2013). Therefore, the lack of correlation between Ce and Eu anomalies and the presence of positive Ce anomaly coexisting with negative Eu anomaly in the study zircons may indicate that the oxygen fugacity is not the only factor controlling Ce^{4+}/Ce^{3+} and Eu^{3+}/Eu^{2+} in magmas (Maas et al., 1992). The plot of Hf versus Ce/Ce^* can also be used to monitor the difference in oxidation state accompanying magma differentiation. The samples in this study show a wide range of Hf and Ce/Ce^* values (Fig. 8b) which may indicate the crystallization of the magma in a variable range of f_{O2} over a long-time interval.

Magma source: mantle versus crust

Zircon can affect the behavior of REE, Y, Th, U, Nb, and Ta, therefore the concentrations and ratios of these trace elements can be used to differentiate zircon from different sources (Li et al., 2014; Wu et al., 2016). In general, zircons from crust-derived magma show higher trace element concentrations as well as Ce-enriched and Eu-depleted REE patterns compared to zircons from mantle-derived magma (Lei et al., 2013). Zircons originating from mantle magmas show negative correlations of Hf with Th, Y and U, in contrast to zircons derived from the crust, which show positive correlations (Wang and Pupin, 1992). In this study, zircons from Ataitir El Dehami granitoids have high REE contents with Ce enrichment and depletion of Eu, which together with the apparent positive correlations between Hf and U, Th, and Y (Figs. 9a, b, and c), suggest that the studied granites were generated from the crust.

In addition, the U/Yb ratio of zircons has been widely used to distinguish zircons crystallizing in magmas of mantle or crustal origin (e.g., Deng et al., 2019; El-Bialy and Ali, 2013; Grimes et al., 2007; Kelemen et al., 2003; Sakyi et al., 2019). Grimes et al. (2007) concluded that the U/Yb ratio of zircons is variable and increases gradually from oceanic gabbro (0.18) to continental granites (1.07) and kimberlite (2.1). Therefore, plotting Hf concentrations versus U/Yb ratios can be used to identify zircon grains from oceanic crust, continental crust, and mantle (Grimes et al., 2007). In Figure 9d, all zircon grains from Ataitir El Dehami granites plotted in the field of the continental crust zircons (Grimes et al., 2007). The high U/Yb, and Gd/Yb ratios of the studied zircons are comparable and have well-defined features of zircons with the arc to within plate signatures (Fig 9e), which is compatible with our geochemical data (Supplementary Fig. 3a and 3b; Pearce, 1996; Maniar and Piccoli, 1989, respectively). Indicated that the Ataitir El Dehami granites can be clearly considered as post-collisional granites.

Crystallization conditions

Yang (2017) proposed an empirical method using CIPW normative quartz (Qtz) and albite (Ab) plus orthoclase (Or) compositions to estimate the emplacement pressure of granite intrusions, referred to as Qtz-geobarometer (Yang et al. 2019, 2021). Using the improved Qtz-geobarometer of Yang et al. (2021), the estimated crystallization pressures of the studied granites fall between 1.9–3.8 Kb, and thus suggest its crystallization depth ranges from 5 to 10 km, assuming that the density of continental crust is 2.7 g/cm^3.

Magma temperature can be estimated using the zircon-saturation model (T_{Zr}) (Watson and Harrison, 1983) that was revised by Boehnke et al. (2013). Zr in the studied granites ranges from 95 to 171 ppm, thus the corresponding T_{Zr} equals 761 to 826°C with an average of 786 °C; Table 2. The results are also in agreement with the temperatures evaluated using P_2O_5–SiO_2 diagram after Harrison and Watson, 1984; (Supplementary Fig. 2c) which indicates that the formation temperature of the studied granites is less than 800 °C. Miller et al. (2003) suggested that the average T_{Zr} for inheritance-rich granitoids is 766°C and 837°C for inheritance-poor granitoids. As a result, the studied rocks are inheritance-rich granitoids, i.e., saturated in zircon at the source, with an average T_{Zr} of 786 °C.

Ti-in-zircon thermometry

Ti can substitute for Zr^{4+} and Si^{4+} in zircon, and the crystallization temperature of zircon has certain constraints on Ti content and element substitution (Watson et al., 2006). Therefore, Ti concentrations in zircon are considered a powerful geochemical tracer utilized to estimate the magmatic temperature of the melt during zircon crystallization (Watson and Harrison, 2005; Ferry and Watson, 2007; Fu et al., 2008).

In this study, most Ti values obtained in magmatic zircons are below 60 ppm, and only zircon with Ti contents ≤ 75 ppm was considered for calculations, as these concentrations are in line with the acceptable range in igneous zircons (Hoskin and Schaltegger, 2003). The magmatic zircon crystallization temperatures ($T_{Ti\text{-}in\text{-}zrc}$) are currently determined by applying the equation of Watson et al. (2006), which states that: $T (K) = 5080 \pm 30 (1 / ((6.01 \pm 0.03) - \log (Ti_{zircon}))$. The application of this equation to the investigated zircons returns temperatures of 607–974 °C (average $T_{Ti\text{-}in\text{-}zrc} = 728$ °C).

U-Pb zircon geochronology

Timing of crystallization

Four samples from Ataitir El Dehami pluton (SI82B, SA9, SA12, SA11) yield younger ages of (580±26 Ma, 596±2.2 Ma, 601±3.9 Ma, 603±15 Ma, respectively), whereas sample SI81C yields two different ages, the youngest age is 575±7.1 Ma and the oldest age is 735± 9 Ma. Zircons of younger ages extracted from this pluton show oscillatory growth zoning and have high Th/U ratios > 0.1, indicate a magmatic origin, and suggesting that the U–Pb ages obtained from these zircons represent the timing of crystallization of this pluton which range from 575±7.1 Ma to 603±15 Ma. Our new ages allowed us to suggest that the magmatic activities continue up to 28My throughout continuous exhumation pulses.

These younger ages have been documented in other areas in Sinai and Eastern Desert. In the Sinai Peninsula, Ali et al. (2009) proposed a progressive sequence of magmatism (between 580 and 595 Ma) from monzogranite to syenogranite to alkali-feldspar granite. For example, the monzogranite at Wadi Lithi has an age of 594 ± 14 Ma, identical to the reported age from a syenogranite sample at Wadi Nasb with an age of 594 ± 8 Ma, but slightly older than the syenogranite of Wadi Ghazala, with an age of 582 ± 6 Ma, whereas the alkali-feldspar granite at Wadi Lithi intrudes the monzogranite and has an age of 579 ± 9 Ma.

Bielski et al. (1979) reported a Rb/Sr whole-rock isochron age of 580 ± 23 Ma for a syenogranite pluton from the Iqna granite at the Wadi Kid area in southeastern Sinai. Gabal Musa, Wadi Lithey and Wadi Um Adawi granites dated with the $^{207}Pb/^{206}Pb$ single zircon stepwise evaporation method at 596 ± 18 Ma and 597 ± 12 Ma, respectively (Abu Anbar et al., 1999). Recently, a syenogranite sample from Wadi Kid yielded a $^{206}Pb/^{238}U$ weighted mean age of 604 ± 5 Ma (Moghazi et al., 2012). The St. Katarina Ring Complex formed over a ~9 My interval from 602 to 593 Ma, (Moreno et al., 2014).

U–Pb zircon geochronology of Abu Harba, and Abu Marwa A-type granite intrusions in the northern Eastern Desert yielded ages of 600.1 ± 8.5Ma, and 601.1 ± 2.4 Ma, respectively (Feteha et al., 2022). Moussa et al., 2008 concluded that the ages of the younger granitoids in the Eastern Desert are as follows: 603 Ma for SED granites (Um Ara), ~597 Ma for CED granites (Al Missikat), and 595–605 Ma for NED granites (Abu Harba, 595 Ma, and Qattar, 605 Ma).

Zircon grain (sample SI81C) with old age reported during this study (735± 9Ma) may be derived from the neighboring arc (740 ± 6.4 Ma) that formed Wadi Seih area (Abu Anbar et al., 2023) which are consisting with the progressive closing of the Mozambique Ocean. This age is correlated to the age of Taba granite gneiss (the northern part of the Taba Metamorphic Complex), which yielded zircon U–Pb ages of 737 ± 9 Ma (Kolodner, 2007). The age of the older source of the present granites overlaps with that of the Nab complex (737 ± 10 Ma; Kozdrój, et al., 2014). This age may overlap also with the oldest magmatic activity along Ajjaj Shear (747 ± 12 Ma), for deformed granodiorite-tonalite plutons (Hassan et al., 2016).

Conclusions and tectonic evolution

The Ataitir El Dehami granites primarily belong to the classification of alkali feldspar granites, with syenogranites occurring rarely. Granitoids display a relatively weakly peraluminous, alkali-calcic, and ferroan A-type nature. They were emplaced in both island arc and within-plate settings (post-collision granites; Supplementary Fig. 3a and 3b; Pearce, 1996; Maniar and Piccoli, 1989, respectively). Granitoids show enrichment in elements such as Rb, Pb, and Th, they exhibit depletion in Ba, Sr, Ti, Nb, and other high field strength elements (HFSEs), resembling crustal or arc magmatic rocks. The Ataitir El Dehami granites classified as A2-granites, they originate from underplated crust or continental crust influenced by island-arc magmatism. Partial melting of the underplated I-type tonalitic source is proposed as the formation mechanism. Zircons extracted from the studied granites exhibit oscillatory growth zoning and high Th/U ratios (>0.1), indicating a magmatic origin. The chondrite-normalized REE patterns of the zircon samples display a steeply-rising slope with significant HREEs enrichment and LREEs depletion. They also exhibit distinct positive Ce and negative Eu anomalies, indicative of their crystallization environments. Negative Eu anomaly attributed to plagioclase fractionation whereas the positive Ce anomaly associated with oxidation processes. Temperature estimates from the Ti-in-zircon thermometer range from 607°C to 974°C with an average 728°C, which is consistent with zircons growing in the continental crust. All zircon grains from Ataitir El Dehami granites indicating their affiliation with continental crust. As well as the studied zircons show well-defined features with arc-within plate signature which is compatible with the geochemical data which indicated that the Ataitir El Dehami granites can be clearly considered as post collisional granites. Crystallization ages for the Ataitir El Dehami granites range from 603 to 575 Ma. LA-ICP-MS zircon U-Pb isotopic analyses reveal the presence of inherited zircon grains likely associated with older crustal rocks, possibly from an island arc regime.

Based on the geochemical and geochronological data, the Ataitir El Dehami granites are post-collisional A-type granites that formed from the partial melting of crustal sources during a transitional tectonic setting from convergence to extension at approximately 600 Ma, as indicated by previous studies (e.g., Stern, 1994; Genna et al., 2002; Jarrar et al., 2003).

The proposed tectonic model for the formation of the Ataitir El Dehami granites (Fig. 10), as outlined in the provided document, involves the following key stages:

1. **Subduction (magma generation)** and **crustal melting stage:** Initially, a period of convergence led to the subduction of a lithospheric mantle beneath the continental crust (Fig. 10a). This process triggered the melting of the asthenosphere, generating magma that formed an arc at nearly 735± 9Ma (Fig. 5e). Following the arc formation, the tectonic regime shifted to a post-collisional setting (Fig. 7f; Supplementary Fig. 3a and 3b). The granites were produced through the partial melting of underplated I-type tonalitic sources (Fig.7e), within the continental crust.

2. **Extension and post collision stage:** The granites were emplaced during a critical transitional period from convergence to extension at around 600 Ma (Fig. 10b). U-Pb zircon dating indicates crystallization ages between 603 and 575 Ma, reflecting a shift from orogenic to anorogenic setting in the region with inherited zircon grains from an older arc dated to 735 Ma.

Acknowledgment

We would like to express our sincere thanks to Prof. Ralf Kryza from Institute of Geological Sciences, Wroclaw University, Poland, for assistance to carry out the microprobe analyses. Grateful thanks also to Prof. Massimo Coltorti from Earth Science Department, Ferrara University, Italy, for analyzing major and trace elements. The authors would like to thank ASRT for providing the project funding (Grant number 9182) and the National Natural Science Foundation of China for supporting a bilateral research project (Grant: 42161144013). Grateful thanks also to Prof. Kamal Ali for reviewing the manuscript. The authors gratefully acknowledge Prof. Yildirim Dilek (Miami University, USA), Prof. Orhan Karsli (Karadeniz Teknik University, Trabzon, Turkey) and Dr. Nargess Shirdashtzadeh (Tarbiat Modares University, Tehran, Iran) for careful and constructive reviews that significantly improved the manuscript.

Appendices

This manuscript includes 5 Supplementary tables and 2 supplementary figures as following,

Supplementary tables S1-S5 for zircon trace element data.

Supplementary Fig. 1 for cross-polarized photomicrographs.

Supplementary Fig. 2 for discrimination diagrams of the studied granitoids.

Supplementary Fig. 3 Chondrite normalized trace element spider diagrams of granite samples (Anders and Grevesse, 1989).

References

Abd El Ghaffar, N.I. and Ramadan, A.A., 2018. Geochemistry and origin of alkaline granites at Wadi Umm Adawi-Yahmid area, south Sinai-Egypt. Journal of African Earth Sciences, 146, pp.66-77.

Abdelfadil, K.M., Obeid, M.A., Azer, M.K. and Asimow, P.D., 2018. Late Neoproterozoic adakitic lavas in the Arabian-Nubian shield, Sinai Peninsula, Egypt. Journal of Asian Earth Sciences, 158, pp.301-323.

Abu Anbar, M.M., 2009. Petrogenesis of the Nesryin gabbroic intrusion in SW Sinai, Egypt: new contributions from mineralogy, geochemistry, Nd and Sr isotopes. Miner. Petrol. 95,87–103.

Abu Anbar, M.M., Ghoneim, M.F., Hassan, A.M. and Pichler, H., 1999. Single zircon dating, zircon typology and oxygen isotopes of alkaline granites from Egypt. In 4th International Conference on the Geology of the Arab World, Cairo University (pp. 417-434).

Abu-Alam, T.S. and Stüwe, K. 2009. Exhumation during oblique transpression: the Feiran–Solaf region, Egypt. Journal of Metamorphic Geology, 27(6), pp.439-459.

Abu-Alam, T.S., Hassan, M., Stüwe, K., Meyer, S.E. and Passchier, C.W., 2014. Multistage tectonism and metamorphism during Gondwana collision: Baladiyah complex, Saudi Arabia. Journal of Petrology, 55(10), pp.1941-1964.

Ali, B.H., Wilde, S.A. and Gabr, M.M.A., 2009. Granitoid evolution in Sinai, Egypt, based on precise SHRIMP U–Pb zircon geochronology. Gondwana Research, 15(1), pp.38-48.

Anbar, M.A., Abu-Alam, T.S., Ghoneim, M.F., Dong, Y., Li, X.H., Ramadan, D.H. and Masoud, A.E., 2023. Rodinia to Gondwana evolution record, South Sinai, Egypt: Geological and geochronological constraints. Precambrian Research, 398, p.107221.

Andersen, T., 2002. Correction of common lead in U–Pb analyses that do not report 204Pb. Chemical geology, 192(1-2), pp.59-79.

Anderson, J.L. and Bender, E.E. 1989. Nature and origin of Proterozoic A-type granitic magmatism in the southwestern United States of America. Lithos, 23(1-2), pp.19-52.

Anders, E. and Grevesse, N. 1989. Abundances of the elements: Meteoritic and solar. Geochimica et Cosmochimica acta, 53(1), pp.197-214.

Azer, M.K. and El-Gharbawy, R.I., 2011. The Neoproterozoic layered mafic–ultramafic intrusion of Gabal Imleih, south Sinai, Egypt: implications of post-collisional magmatism in the north Arabian–Nubian Shield. Journal of African Earth Sciences, 60(4), pp.253-272.

Azer, M.K., Abdelfadil, K.M., Ramadan, A.A., 2019. Geochemistry and Petrogenesis of Late Ediacaran Rare-Metal Albite Granite of the Nubian Shield: Case Study of Nuweibi Intrusion, Eastern Desert, Egypt. The Journal of Geology, 127: 665-689. Bacon, C.R., and Druitt, T.H., 1988. Compositional evolution of the zoned calcalkaline magma chamber of Mount Mazama, Crater Lake, Oregon. Contributions to Mineralogy and Petrology, 98: 224–256.

Barbarin, B. 1999. A review of the relationships between granitoid types, their origins and their geodynamic environments. Lithos, 46(3), pp.605-626.

Barth, A.P. and Wooden, J.L. 2010. Coupled elemental and isotopic analyses of polygenetic zircons from granitic rocks by ion microprobe, with implications for melt evolution and the sources of granitic magmas. Chemical Geology, 277(1-2), pp.149-159.

Be'eri-Shlevin, Y., Samuel, M.D., Azer, M.K., Rämö, O.T., Whitehouse, M.J. and Moussa, H.E. 2011. The Ediacaran Ferani and Rutig volcano-sedimentary successions of the northernmost Arabian-Nubian Shield (ANS): new insights from zircon U–Pb geochronology, geochemistry and O–Nd isotope ratios. Precambrian Research, 188(1-4), pp.21-44.

Bea, F., Abu-Anbar, M., Montero, P., Peres, P. and Talavera, C. 2009. The∼ 844 Ma Moneiga quartz-diorites of the Sinai, Egypt: evidence for Andean-type arc or rift-related magmatism in the Arabian-Nubian Shield?. Precambrian Research, 175(1-4), pp.161-168.

Belousova, E.A., Griffin, W.L., O'Reilly, S.Y. and Fisher, N.L. 2002. Igneous zircon: trace element composition as an indicator of source rock type. Contributions to mineralogy and petrology, 143, pp.602-622.

Bentor, Y.K. 1985. The crustal evolution of the Arabo-Nubian Massif with special reference to the Sinai Peninsula. Precambrian research, 28(1), pp.1-74.

Beyth, M., Stern, R.J., Altherr, R. and Kröner, A. 1994. The late Precambrian Timna igneous complex, southern Israel: evidence for comagmatic-type sanukitoid monzodiorite and alkali granite magma. Lithos, 31(3-4), pp.103-124.

Bielski, M., Jäger, E. and Steinitz, G. 1979. The geochronology of Iqna granite (Wadi Kid pluton), southern Sinai. Contributions to Mineralogy and Petrology, 70, pp.159-165.

Boehnke, P., Watson, E.B., Trail, D., Harrison, T.M. and Schmitt, A.K. 2013. Zircon saturation re-revisited. Chemical Geology, 351, pp.324-334.

Bonin, B. 2007. A-type granites and related rocks: evolution of a concept, problems and prospects. Lithos, 97(1-2), pp.1-29.

Brown, G.C., Thorpe, R.S. and Webb, P.C. 1984. The geochemical characteristics of granitoids in contrasting arcs and comments on magma sources. Journal of the Geological Society, 141(3), pp.413-426.

Burnham, A.D. and Berry, A.J. 2012. An experimental study of trace element partitioning between zircon and melt as a function of oxygen fugacity. Geochimica et Cosmochimica Acta, 95, pp.196-212.

Cao, X., Lü, X., Liu, S., Zhang, P., Gao, X., Chen, C. and Mo, Y. 2011. LA-ICP-MS zircon dating, geochemistry, petrogenesis and tectonic implications of the Dapingliang Neoproterozoic granites at Kuluketage block, NW China. Precambrian Research, 186(1-4), pp.205-219.

Cao, Y., Li, S., Zhang, H., Ao, C., Li, Z. and Liu, X. 2010. Laser probe 40 Ar/39 Ar dating for quartz from auriferous quartz veins in the Shihu gold deposit, western Hebei Province, North China. Chinese Journal of Geochemistry, 29, pp.438-445.

Cavosie, A.J., Valley, J.W. and Wilde, S.A. 2006. Correlated microanalysis of zircon: Trace element, δ18O, and U–Th–Pb isotopic constraints on the igneous origin of complex> 3900 Ma detrital grains. Geochimica et Cosmochimica Acta, 70(22), pp.5601-5616.

Chappell, B.W. 1999. Aluminium saturation in I-and S-type granites and the characterization of fractionated haplogranites. Lithos, 46(3), pp.535-551.

Chappell, B.W., Bryant, C.J. and Wyborn, D. 2012. Peraluminous I-type granites. Lithos, 153, pp.142-153.

Chappell, B.W. and White, A.J.R. 1992. I-and S-type granites in the Lachlan Fold Belt. Earth and Environmental Science Transactions of the Royal Society of Edinburgh, 83(1-2), pp.1-26.

Clemens, J.D. 2003. S-type granitic magmas—petrogenetic issues, models and evidence. Earth-Science Reviews, 61(1-2), pp.1-18.

Clemens, J.D., Holloway, J.R. and White, A.J.R. 1986. Origin of an A-type granite; experimental constraints. American mineralogist, 71(3-4), pp.317-324.

Collins, W.J., Beams, S.D., White, A.J.R. and Chappell, B.W. 1982. Nature and origin of A-type granites with particular reference to southeastern Australia. Contributions to mineralogy and petrology, 80, pp.189-200.

Collins, W.J., Murphy, J.B., Blereau, E. and Huang, H.Q. 2021. Water availability controls crustal melting temperatures. Lithos, 402, p.106351.

Corfu, F., Hanchar, J.M., Hoskin, P.W. and Kinny, P. 2003. Atlas of zircon textures. Reviews in mineralogy and geochemistry, 53(1), pp.469-500.

Creaser, R.A., Price, R.C. and Wormald, R.J. 1991. A-type granites revisited: assessment of a residual-source model. Geology, 19(2), pp.163-166.

Dilek, Y. and Ahmed, Z. 2003. Proterozoic ophiolites of the Arabian Shield and their significance in Precambrian tectonics. Geological Society, London, Special Publications, 218(1), pp.685-700.

De la Roche, H.D., Leterrier, J.T., Grandclaude, P. and Marchal, M. 1980. A classification of volcanic and plutonic rocks using R1R2-diagram and major-element analyses—its relationships with current nomenclature. Chemical geology, 29(1-4), pp.183-210.

Deer, W.A., Howie, R.A. and Zussman, J. 1978. Rock-forming minerals. 2A, single chain silicates. Longman, London, 668 P.

Deng, C., Sun, G., Sun, D., Han, J., Yang, D. and Tang, Z. 2019. Morphology, trace elements, and geochronology of zircons from monzogranite in the Northeast Xing'an Block, northeastern China: constraints on the genesis of the host magma. Mineralogy and Petrology, 113, pp.651-666.

Dilles, J.H., Kent, A.J., Wooden, J.L., Tosdal, R.M., Koleszar, A., Lee, R.G. and Farmer, L.P. 2015. Zircon compositional evidence for sulfur-degassing from ore-forming arc magmas. Economic Geology, 110(1), pp.241-251.

Dong, Y., Ge, W., Tian, D., Ji, Z., Yang, H., Bi, J., Wu, H. and Hao, Y. 2019. Geochronology and geochemistry of early cretaceous granitic plutons in the Xing'an Massif, Great Xing'an Range, NE China: Petrogenesis and tectonic implications. Acta Geologica Sinica-English Edition, 93(5), pp.1500-1521.

Eby, G.N. 1990. The A-type granitoids: a review of their occurrence and chemical characteristics and speculations on their petrogenesis. Lithos, 26(1-2), pp.115-134.

Eby, G.N. 1992. Chemical subdivision of the A-type granitoids: petrogenetic and tectonic implications. Geology, 20(7), pp.641-644.

El-Bialy, M.Z. 2010. On the Pan-African transition of the Arabian–Nubian Shield from compression to extension: the post-collision Dokhan volcanic suite of Kid-Malhak region, Sinai, Egypt. Gondwana Research, 17(1), pp.26-43.

El-Bialy, M.Z. and Ali, K.A. 2013. Zircon trace element geochemical constraints on the evolution of the Ediacaran (600–614 Ma) post-collisional Dokhan Volcanics and Younger Granites of SE Sinai, NE Arabian–Nubian Shield. Chemical Geology, 360, pp.54-73.

El-Bialy, M.Z. and Omar, M.M. 2015. Spatial association of Neoproterozoic continental arc I-type and post-collision A-type granitoids in the Arabian–Nubian Shield: the Wadi Al-Baroud older and younger granites, north eastern desert, Egypt. Journal of African Earth Sciences, 103, pp.1-29.

El-Bialy, M., Eliwa, H., Mahdy, N., Murata, M., El-Gameel, K., Sehsah, H., Omar, M., Kato, Y., Fujinaga, K., Andresen, A., 2020. U-Pb zircon geochronology and geochemical constraints on the Ediacaran continental arc and post-collision granites of Wadi Hawashiya, North Eastern Desert, Egypt:

insights into the~ 600 Ma crust-forming event in the northernmost part of Arabian-Nubian Shield. Precambrian Research: 105777.

Ewart, A., Marsh, J.S., Milner, S.C., Duncan, A.R., Kamber, B.S. and Armstrong, R.A. 2004. Petrology and geochemistry of Early Cretaceous bimodal continental flood volcanism of the NW Etendeka, Namibia. Part 1: Introduction, mafic lavas and re-evaluation of mantle source components. Journal of Petrology, 45(1), pp.59-105.

Eyal, M. and Hezkiyahu, T. 1980. Katherina pluton: the outline of a petrologic framework. Israel Journal of Earth Science, 29, 41-52.

Eyal, M., Litvinovsky, B., Jahn, B.M., Zanvilevich, A. and Katzir, Y. 2010. Origin and evolution of post-collisional magmatism: coeval Neoproterozoic calc-alkaline and alkaline suites of the Sinai Peninsula. Chemical Geology, 269(3-4), pp.153-179.

Farahat, E.S. and Azer, M.K. 2011. Post-collisional magmatism in the northern Arabian-Nubian Shield: the geotectonic evolution of the alkaline suite at Gebel Tarbush area, south Sinai, Egypt. Geochemistry, 71(3), pp.247-266.

Ferry, J.M. and Watson, E.B. 2007. New thermodynamic models and revised calibrations for the Ti-in-zircon and Zr-in-rutile thermometers. Contributions to Mineralogy and Petrology, 154(4), pp.429-437.

Feteha, B.F., Lentz, D.R., El Bouseily, A.M., Khalil, K.I., Khamis, H.A. and Moghazi, A.K.M. 2022. Petrogenesis of neoproterozoic Mo-bearing A-type granites in the Gattar area, northern Eastern Desert, Egypt: Implications for magmatic evolution and mineralization processes. Ore Geology Reviews, 148, p.105007.

Foley, S.F., Barth, M.G. and Jenner, G.A. 2000. Rutile/melt partition coefficients for trace elements and an assessment of the influence of rutile on the trace element characteristics of subduction zone magmas. Geochimica et Cosmochimica Acta, 64(5), pp.933-938.

Foster, M.D. 1960. Interpretation of the composition of trioctahedral mica. U.S. Geol Surv Prof Pap 354-B:11–49.

Frost, B.R., Barnes, C.G., Collins, W.J., Arculus, R.J., Ellis, D.J. and Frost, C.D. 2001. A geochemical classification for granitic rocks. Journal of petrology, 42(11), pp.2033-2048.

Frost, B.R. and Frost, C.D. 2008. A geochemical classification for feldspathic igneous rocks. Journal of Petrology, 49(11), pp.1955-1969.

Fu, B., Mernagh, T.P., Kita, N.T., Kemp, A.I. and Valley, J.W. 2009. Distinguishing magmatic zircon from hydrothermal zircon: a case study from the Gidginbung high-sulphidation Au–Ag–(Cu) deposit, SE Australia. Chemical Geology, 259(3-4), pp.131-142.

Fu, B., Page, F.Z., Cavosie, A.J., Fournelle, J., Kita, N.T., Lackey, J.S., Wilde, S.A. and Valley, J.W. 2008. Ti-in-zircon thermometry: applications and limitations. Contributions to Mineralogy and Petrology, 156(2), pp.197-215.

Gamal El Dien, H., Li, Z.X., Abu Anbar, M., Doucet, L.S., Murphy, J.B., Evans, N.J., Xia, X.P. and Li, J. 2021. The largest plagiogranite on Earth formed by re-melting of juvenile proto-continental crust. Communications Earth & Environment, 2(1), p.138.

Genna, A., Nehlig, P., Le Goff, E., Guerrot, C. and Shanti, M.J.P.R. 2002. Proterozoic tectonism of the Arabian Shield. Precambrian Research, 117(1-2), pp.21-40.

Grimes, C.B., John, B.E., Kelemen, P.B., Mazdab, F.K., Wooden, J.L., Cheadle, M.J., Hanghøj, K. and Schwartz, J.J. 2007. Trace element chemistry of zircons from oceanic crust: A method for distinguishing detrital zircon provenance. Geology, 35(7), pp.643-646.

Grimes, C.B., Wooden, J.L., Cheadle, M.J. and John, B.E. 2015. "Fingerprinting" tectono-magmatic provenance using trace elements in igneous zircon. Contributions to Mineralogy and Petrology, 170, pp.1-26.

Halliday, A.N., Davidson, J.P., Hildreth, W. and Holden, P. 1991. Modelling the petrogenesis of high Rb/Sr silicic magmas. Chemical Geology, 92(1-3), pp.107-114.

Harrison, T.M. and Watson, E.B. 1984. The behavior of apatite during crustal anatexis: equilibrium and kinetic considerations. Geochimica et cosmochimica acta, 48(7), pp.1467-1477.

Hassan, M., Stüwe, K., Abu-Alam, T.S., Klötzli, U. and Tiepolo, M. 2016. Time constraints on deformation of the Ajjaj branch of one of the largest Proterozoic shear zones on Earth: The Najd Fault System. Gondwana Research, 34, pp.346-362.

Hassan, M.A. and Hashad, A.H. 1990. Precambrian of Egypt. In: Said, R. (Ed.), The Geology of Egypt. Balkema, Rotterdam, pp. 201–248.

Hey, M.H. 1954. A new review of the chlorites. Mineral. Mag. J. Mineral. Soc. 30 (224), 277–292.

Hoskin, P.W. and Schaltegger, U. 2003. The composition of zircon and igneous and metamorphic petrogenesis. Reviews in mineralogy and geochemistry, 53(1), pp.27-62.

Hoskin, P.W. 2005. Trace-element composition of hydrothermal zircon and the alteration of Hadean zircon from the Jack Hills, Australia. Geochimica et cosmochimica acta, 69(3), pp.637-648.

Hoskin, P.W. and Ireland, T.R. 2000. Rare earth element chemistry of zircon and its use as a provenance indicator. Geology, 28(7), pp.627-630.

Hu, Z.L., Wang, X.W., Qin, Z.P., Zhang, J., Gao, Y. and Peng, H. 2012. Basic characteristics of zircon trace elements and their genetic significances in Jiama copper polymetallic deposit. Nonferrous Metals (Min. Sect.), 64, pp.58-63.

Huang, H.Q., Li, X.H., Li, W.X. and Li, Z.X. 2011. Formation of high δ18O fayalite-bearing A-type granite by high-temperature melting of granulitic metasedimentary rocks, southern China. Geology, 39(10), pp.903-906.

Jarrar, G., Stern, R.J., Saffarini, G. and Al-Zubi, H. 2003. Late-and post-orogenic Neoproterozoic intrusions of Jordan: implications for crustal growth in the northernmost segment of the East African Orogen. Precambr. Res. 123 (2–4), 295–319.

Jarrar, G.H., Manton, W.I., Stern, R.J. and Zachmann, D. 2008. Late Neoproterozoic A-type granites in the northernmost Arabian-Nubian Shield formed by fractionation of basaltic melts. Geochemistry, 68(3), pp.295-312.

Johnson, P.R., Andresen, A., Collins, A.S., Fowler, A.R., Fritz, H., Ghebreab, W. and Stern, R. J. 2011. Late Cryogenian-Ediacaran history of the Arabian-Nubian Shield: a review of depositional, plutonic, structural, and tectonic events in the closing stages of the northern East African Orogen. J. Afr. Earth Sc. 61 (3), 167–232.

Johnson, P.R. and Woldehaimanot, B. 2003. Development of the Arabian-Nubian Shield: perspectives on accretion and deformation in the northern East African Orogen and the assembly of Gondwana. Geol. Soc. Lond. Spec. Publ. 206 (1), 289–325.

Kelemen, P.B., Hanghøj, K. and Greene, A.R. 2003. One view of the geochemistry of subduction-related magmatic arcs, with an emphasis on primitive andesite and lower crust. Treatise on geochemistry, 3, p.659.

Kelemen, P.B., Johnson, K.T.M., Kinzler, R.J. and Irving, A.J. 1990. High-field-strength element depletions in arc basalts due to mantle–magma interaction. Nature, 345(6275), pp.521-524.

King, P.L., White, A.J.R., Chappell, B.W. and Allen, C.M. 1997. Characterization and origin of aluminous A-type granites from the Lachlan Fold Belt, southeastern Australia. Journal of petrology, 38(3), pp.371-391.

Kirkland, C.L., Smithies, R.H., Taylor, R.J.M., Evans, N. and McDonald, B. 2015. Zircon Th/U ratios in magmatic environs. Lithos, 212, pp.397-414.

Kolodner, K. 2007. the Provenance of the Siliciclastic Section in Israel and Jordan: U-Pb Dating of Detrital Zircons. The Hebrew University of Jerusalem, Jerusalem 133.

Konopelko, D., Biske, G., Seltmann, R., Eklund, O. and Belyatsky, B. 2007. Hercynian post-collisional A-type granites of the Kokshaal Range, southern Tien Shan, Kyrgyzstan. Lithos, 97(1-2), pp.140-160.

Kozdrój, W., Kennedy, A., Johnson, P.R., Ziółkowska-Kozdrój, M. and Kadi, K. 2014. SHRIMP U-Pb zircon geochronological constraints on Cryogenian-Ediacaran tectonomagmatic events in the northwestern Arabian Shield. In EGU General Assembly Conference Abstracts (p. 1710).

Lachance, G. and Traill, R. 1966. The theoretical influence coefficient method. Spectrosc 11, 43–48.

Laurent, O., Martin, H., Moyen, J.F. and Doucelance, R. 2014. The diversity and evolution of late-Archean granitoids: Evidence for the onset of “modern-style” plate tectonics between 3.0 and 2.5 Ga. Lithos, 205, pp.208-235.

Lei, W.Y., Shi, G.H. and Liu, Y.X. 2013. Research progress on trace element characteristics of zircons of different origins. Earth Science Frontiers, 20(4), pp.273-284.

Li, H., Palinkaš, L.A., Watanabe, K. and Xi, X.S. 2018. Petrogenesis of Jurassic A-type granites associated with Cu-Mo and W-Sn deposits in the central Nanling region, South China: Relation to mantle upwelling and intra-continental extension. Ore Geology Reviews, 92, pp.449-462.

Li, H., Watanabe, K. and Yonezu, K. 2014. Zircon morphology, geochronology and trace element geochemistry of the granites from the Huangshaping polymetallic deposit, South China: Implications for the magmatic evolution and mineralization processes. Ore Geology Reviews, 60, pp.14-35.

Liu, X., Gao, S., Diwu, C., Yuan, H. and Hu, Z. 2007. Simultaneous in-situ determination of U-Pb age and trace elements in zircon by LA-ICP-MS in 20 μm spot size. Chinese Science Bulletin, 52(9), pp.1257-1264.

Loader, M.A., Wilkinson, J.J. and Armstrong, R.N. 2017. The effect of titanite crystallisation on Eu and Ce anomalies in zircon and its implications for the assessment of porphyry Cu deposit fertility. Earth and Planetary Science Letters, 472, pp.107-119.

Loucks, R.R., Fiorentini, M.L. and Henríquez, G.J. 2020. New magmatic oxybarometer using trace elements in zircon. Journal of Petrology, 61(3), p. egaa034.

Lu, Y.J., Loucks, R.R., Fiorentini, M., McCuaig, T.C., Evans, N.J., Yang, Z.M., Hou, Z.Q., Kirkland, C.L., Parra-Avila, L.A. and Kobussen, A. 2016. Zircon compositions as a pathfinder for porphyry Cu±Mo±Au deposits.

Maas, R., Kinny, P.D., Williams, I.S., Froude, D.O. and Compston, W. 1992. The Earth's oldest known crust: a geochronological and geochemical study of 3900–4200 Ma old detrital zircons from Mt. Narryer and Jack Hills, Western Australia. Geochimica et Cosmochimica Acta, 56(3), pp.1281-1300.

Maniar, P.D. and Piccoli, P.M. 1989. Tectonic discrimination of granitoids. Geological society of America bulletin, 101(5), pp.635-643.

Middlemost, E.A. 1994. Naming materials in the magma/igneous rock system. Earth-science reviews, 37(3-4), pp.215-224.

Miller, S.D., Duncan, B.L., Brown, J., Sparks, J.A. and Claud, D.A. 2003. The outcome rating scale: A preliminary study of the reliability, validity, and feasibility of a brief visual analog measure. Journal of brief Therapy, 2(2), pp.91-100.

Moghazi, A.M. 2002. Petrology and geochemistry of Pan-African granitoids, Kab Amiri area, Egypt–implications for tectonomagmatic stages in the Nubian Shield evolution. Mineralogy and Petrology, 75, pp.41-67.

Moreno, J.A., Molina, J.F., Montero, P., Anbar, M.A., Scarrow, J.H., Cambeses, A. and Bea, F. 2014. Unraveling sources of A-type magmas in juvenile continental crust: constraints from compositionally diverse Ediacaran post-collisional granitoids in the Katerina Ring Complex, southern Sinai, Egypt. Lithos, 192, pp.56-85.

Moussa, E.M., Stern, R.J., Manton, W.I. and Ali, K.A. 2008. SHRIMP zircon dating and Sm/Nd isotopic investigations of Neoproterozoic granitoids, Eastern Desert, Egypt. Precambrian Research, 160(3-4), pp.341-356.

Nehlig, P., Genna, A., Asfirane, F., BRGM, France, Guerrot, C., Eberlé, J.M., Kluyver, H.M., Lasserre, J.L., Le Goff, E., Nicol, N. and BRGM, France, 2002. A review of the Pan-African evolution of the Arabian Shield. GeoArabia, 7(1), pp.103-124.

Orejana, D., Villaseca, C., Armstrong, R.A. and Jeffries, T.E. 2011. Geochronology and trace element chemistry of zircon and garnet from granulite xenoliths: constraints on the tectonothermal evolution of the lower crust under central Spain. Lithos, 124(1-2), pp.103-116.

Pearce, J. 1996. Sources and settings of granitic rocks. Episodes Journal of International Geoscience, 19(4), pp.120-125.

Pearce, J.A., Harris, N.B. and Tindle, A.G. 1984. Trace element discrimination diagrams for the tectonic interpretation of granitic rocks. Journal of petrology, 25(4), pp.956-983.

Peccerillo, A. and Taylor, S.R. 1976. Geochemistry of Eocene calc-alkaline volcanic rocks from the Kastamonu area, northern Turkey. Contributions to mineralogy and petrology, 58, pp.63-81.

Peng, P., Anbar, M.M.A., He, X.F., Liu, X. and Qin, Z. 2022. Cryogenian accretion of the Northern Arabian-Nubian shield: integrated evidence from central Eastern Desert Egypt. Precambrian Research, 371, p.106599.

Richard, L.R. 1995. MinPet: Mineralogical and Petrological Data Processing System, Version 2.02. MinPet Geological Software, Qu´ebec.

Rieder, M., Cavazzini, G., D'yakonov, Y.S., Frank-Kamenetskii, V.A., Gottardi, G., Guggenheim, S., Koval, P.W., Müller, G., Neiva, A.M., Radoslovich, E.W. and Robert, J.L. 1998. Nomenclature of the micas. Clays and clay minerals, 46(5), pp.586-595.

Rubatto, D. 2002. Zircon trace element geochemistry: partitioning with garnet and the link between U–Pb ages and metamorphism. Chemical geology, 184(1-2), pp.123-138.

Rubatto, D. 2017. Zircon: the metamorphic mineral. Reviews in mineralogy and geochemistry, 83(1), pp.261-295.

Sakyi, A.P., Su, B., Kwayisi, D., Chen, C., Bai, Y. and Alemayehu, M. 2019. Zircon Trace Element Constraints on the Evolution of the Paleoproterozoic Birimian Granitoids of the West African Craton (Ghana). Journal of Earth Science, 29, 43-56.

Sami, M., Ntaflos, T., Farahat, E.S., Mohamed, H.A., Ahmed, A.F. and Hauzenberger, C. 2017. Mineralogical, geochemical and Sr-Nd isotopes characteristics of fluorite-bearing granites in the Northern Arabian-Nubian Shield, Egypt: Constraints on petrogenesis and evolution of their associated rare metal mineralization. Ore Geology Reviews, 88, pp.1-22.

Sami, M., Ntaflos, T., Farahat, E.S., Mohamed, H.A., Hauzenberger, C. and Ahmed, A.F. 2018. Petrogenesis and geodynamic implications of Ediacaran highly fractionated A-type granitoids in the north Arabian-Nubian Shield (Egypt): Constraints from whole-rock geochemistry and Sr-Nd isotopes. Lithos, 304, pp.329-346.

Schaltegger, U. 2007. Hydrothermal zircon. Elements, 3(1), pp.51-79.

Sheng, Y.M., Zheng, Y.F., Chen, R.X., Li, Q. and Dai, M., 2012. Fluid action on zircon growth and recrystallization during quartz veining within UHP eclogite: Insights from U–Pb ages, O–Hf isotopes and trace elements. Lithos, 136, pp.126-144.

Stern, R.J. 1994. Arc assembly and continental collision in the Neoproterozoic East African Orogen: implications for the consolidation of Gondwanaland. Annu. Rev. Earth Planet. Sci. 22 (1), 319–351.

Stern, R.J. 2002. Subduction zones. Reviews of geophysics, 40(4), pp.3-1.

Stern, R.J. 2008. Modern-style plate tectonics began in Neoproterozoic time: An alternative interpretation of Earth's tectonic history. When did plate tectonics begin on planet Earth 265, 280.

Stern, R.J. and Gottfried, D. 1986. Petrogenesis of a late Precambrian (575–600 Ma) bimodal suite in northeast Africa. Contributions to Mineralogy and Petrology, 92(4), pp.492-501.

Stern, R.J. and Hedge, C.E. 1985. Geochronologic and isotopic constraints on late Precambrian crustal evolution in the Eastern Desert of Egypt. American Journal of Science, 285(2), pp.97-127.

Stern, R.J. and Johnson, P. 2010. Continental lithosphere of the Arabian Plate: a geologic, petrologic, and geophysical synthesis. Earth Sci. Rev. 101 (1–2), 29–67.

Stoeser, D.B. and Frost, C.D. 2006. Nd, Pb, Sr, and O isotopic characterization of Saudi Arabian shield terranes. Chemical Geology, 226(3-4), pp.163-188.

Sun, S.S. and McDonough, W.F. 1989. Chemical and isotopic systematics of oceanic basalts: implications for mantle composition and processes. Geological Society, London, Special Publications, 42(1), pp.313-345.

Sylvester, P.J. 1989. Post-collisional alkaline granites. The Journal of Geology, 97(3), pp.261-280.

Thornton, C.P. and Tuttle, O.F. 1960. Chemistry of igneous rocks–[Part] 1, Differentiation index. American Journal of Science, 258(9), pp.664-684.

Trail, D., Watson, E.B. and Tailby, N.D. 2012. Ce and Eu anomalies in zircon as proxies for the oxidation state of magmas. Geochimica et cosmochimica acta, 97, pp.70-87.

Turner, S.P., Foden, J.D. and Morrison, R.S. 1992. Derivation of some A-type magmas by fractionation of basaltic magma: an example from the Padthaway Ridge, South Australia. Lithos, 28(2), pp.151-179.

Wang, F., Liu, S.A., Li, S. and He, Y. 2013. Contrasting zircon Hf–O isotopes and trace elements between ore-bearing and ore-barren adakitic rocks in central-eastern China: implications for genetic relation to Cu–Au mineralization. Lithos, 156, pp.97-111.

Wang, Q., Zhu, D.C., Zhao, Z.D., Guan, Q., Zhang, X.Q., Sui, Q.L., Hu, Z.C. and Mo, X.X. 2012. Magmatic zircons from I-, S-and A-type granitoids in Tibet: Trace element characteristics and their application to detrital zircon provenance study. Journal of Asian Earth Sciences, 53, pp.59-66.

Watson, E.B. and Harrison, T.M. 1983. Zircon saturation revisited: temperature and composition effects in a variety of crustal magma types. earth and planetary science letters, 64(2), pp.295-304.

Watson, E.B. and Harrison, T.M. 2005. Zircon thermometer reveals minimum melting conditions on earliest Earth. Science, 308(5723), pp.841-844.

Watson, E.B., Wark, D.A. and Thomas, J.B. 2006. Crystallization thermometers for zircon and rutile. Contributions to Mineralogy and Petrology, 151(4), pp.413-433.

Whalen, J.B., Currie, K.L. and Chappell, B.W. 1987. A-type granites: geochemical characteristics, discrimination and petrogenesis. Contributions to mineralogy and petrology, 95, pp.407-419.

Wu, F.Y., Li, X.H., Zheng, Y.F. and Gao, S. 2007. Lu-Hf isotopic systematics and their applications in petrology. Acta Pet Sin, 23(2), pp.185–22.

Wu, T., Xiao, L. and Ma, C. 2016. U-Pb geochronology of detrital and inherited zircons in the Yidun arc belt, eastern Tibet Plateau and its tectonic implications. Journal of Earth Science, 27, pp.461-473.

Xia, Q.X., Zheng, Y.F. and Hu, Z.c2010. Trace elements in zircon and coexisting minerals from low-T/UHP metagranite in the Dabie orogen: implications for action of supercritical fluid during continental subduction-zone metamorphism. Lithos, 114(3-4), pp.385-412.

Xiang, W. and Pupin, J.P., 1992. Distribution characteristics of trace elements in zircons from granitic rocks. Chinese Journal of Geology, 27(2), pp.131-140.

Yang, J.H., Wu, F.Y., Wilde, S.A., Xie, L.W., Yang, Y.H. and Liu, X.M. 2007. Tracing magma mixing in granite genesis: in situ U–Pb dating and Hf-isotope analysis of zircons. Contributions to Mineralogy and Petrology, 153, pp.177-190.

Yang, W.B., Niu, H.C., Shan, Q., Sun, W.D., Zhang, H., Li, N.B., Jiang, Y.H. and Yu, X.Y. 2014. Geochemistry of magmatic and hydrothermal zircon from the highly evolved Baerzhe alkaline granite: implications for Zr–REE–Nb mineralization. Mineralium Deposita, 49, pp.451-470.

Yang, X.M. 2007. Using the Rittmann Serial Index to define the alkalinity of igneous rocks. Neues Jahrbuch fur Mineralogie-Abhandlungen, 184(1), pp.95-104.

Yang, X.M., Drayson, D. and Polat, A. 2019. S-type granites in the western Superior Province: a marker of Archean collision zones. Canadian Journal of Earth Sciences, 56(12), pp.1409-1436.

Yang, X.M., Lentz, D.R. and Chi, G. 2021. Ferric-ferrous iron oxide ratios: Effect on crystallization pressure of granites estimated by Qtz-geobarometry. Lithos, 380, p.105920.

Zhao, D., Ge, W., Yang, H., Dong, Y., Bi, J. and He, Y. 2018. Petrology, geochemistry, and zircon U–Pb–Hf isotopes of Late Triassic enclaves and host granitoids at the southeastern margin of the Songnen–Zhangguangcai Range Massif, Northeast China: Evidence for magma mixing during subduction of the Mudanjiang oceanic plate. Lithos, 312, pp.358-374.

List of figures

Fig. 1. (a) Metamorphic belts in south Sinai (after Eyal and Hezkiyahu, 1980**),** (b) Geological map of the district around Ataitir El Dehami granites, Southwest Sinai, Egypt

Fig. 2. Photograph of G. Ataitir El Dehami granites. (a) G. Ataitir El Dehami granites shows high to moderate relief with a pinkish white color, (b and c) Discordant sharp contact between gneisses and granites, (d) G. Ataitir El Dehami granites cut by basic dykes trending NE-SW.

Fig. 3. Major element geochemical characteristics of Ataitir El Dehami granitic rocks, (a) Total Alkali vs. silica (TAS) classification diagram (Middlemost.,1994), (b) R1-R2 classification diagram (De La Roche et al. 1980), (c) K_2O vs SiO_2 diagram (Peccerillo and Taylor, 1976), (d) $Al_2O_3/(Na_2O+K_2O)$ versus $Al_2O_3/(CaO+ Na_2O+K_2O)$ diagram for the studied granites (Maniar and Piccoli, 1989) , (e) discrimination diagram of Sylvester (1989) for rocks with > 68 wt. % SiO_2, (f) MALI (modified alkaline lime index) versus SiO_2 diagram (Frost et al., 2001; Frost and Frost, 2008), (g) FeOt /(FeOt + MgO) versus SiO_2 diagram (Frost et al., 2001), (h) Primitive mantle normalized diagram (Sun and McDonough, 1989).

Fig. 4. Cathodlimenscence image of zircon for the present granite samples.

Fig. 5. U-Pb zircon Concordia diagrams for the present granite samples.

Fig. 6. Plots of chondrite-normalized (Anders and Grevesse, 1989) REE content in zircons from the studied granites.

Fig. 7. Discrimination diagrams of the studied granitoids, (a) Na_2O vs. K_2O diagram (Collins et al., 1982), (b) $Na_2O + K_2O/CaO$ vs. 10^{*4} Ga/Al diagram (Whalen et al., 1987), (c) $Na_2O + K_2O/CaO$ vs. (Zr + Nb+ Ce+ Y) diagram (Whalen et al., 1987), (d) Y-Nb-3Ga diagram (Eby, 1992), (e) Ternary diagram of $Al_2O_3/(FeOt + MgO)$ - 3CaO - $5(K_2O/Na_2O)$ (Laurent et al. 2014), (f) Nb versus Y diagram (Pearce et al., 1984).

Fig. 8. Plots of (a) Ce/Ce* vs. Eu/Eu* and (b) Hf vs. Ce/Ce* revealing the oxidation state of the magma from which the studied zircons were crystallized.

Fig. 9. Plots of (a) Hf vs. U, (b) Hf vs. Th, (c) Hf vs. Y for the studied zircons, (d) Hf vs. U/Yb, (e) Gd/Yb vs. U/Yb diagram (Grimes et al., 2015) with fields after Gamal El Dien et al. (2021).

Fig. 10. A proposed schematic diagram for the tectonic evolution of Ataitir El Dehami granites, (a) Subduction (magma generation) and crustal melting stage and (b) Extension and post collision stage.

List of tables

Table 1. Representative plagioclase, biotite and chlorite microprobe analyses.

Table 2. Chemical analyses of the studied granites and some parameters.

Table 3. LA-ICP-MS zircon U-Pb data for Ataitir El Dehami granites.

Table 1

Mineral	Plagioclase				Biotite						Chlorite			
Analyses/Sa.No	SA12-c	SA12-f	SA12-e	SA12-d	Analyses/Sa.No	SA12-f	SA12-e	SA12-a	SA12-b	Analyses/Sa.No	SA12-c	SA12-d	SA12-a	SA12-b
Core/rim	c	r	c	r							c	r	c	r
SiO_2	68.69	66.94	66.09	65.15	SiO_2	34.83	31.17	26.52	41.71	SiO2	27.09	24.60	24.52	24.55
Al_2O_3	17.70	23.29	20.91	21.28	TiO_2	1.88	2.55	0.42	0.94	TiO2	0.35	0.15	0.05	0.07
Fe_2O_3	0.00	0.03	0.13	0.19	$Al2O_3$	15.58	17.79	18.34	17.53	Al2O3	16.77	17.02	15.44	17.39
MgO	0.02	0.05	0.02	0.05	FeO	30.20	33.85	39.89	23.50	FeO	42.25	43.77	43.79	43.88
MnO	0.00	0.00	0.02	0.00	MnO	0.49	0.35	0.43	0.19	MnO	0.47	0.47	0.53	0.57
CaO	1.07	0.26	1.68	0.39	MgO	0.97	1.33	1.72	0.88	MgO	1.68	1.77	1.81	1.69
Na_2O	11.94	10.47	10.34	10.16	CaO	0.14	0.14	0.18	0.06	CaO	0.14	0.04	0.09	0.07
K_2O	0.09	0.24	0.39	1.51	Na2O	0.18	0.17	0.17	0.14	Na2O	0.16	0.02	0.04	0.06
Total	99.51	101.28	99.58	98.73	K2O	9.76	6.58	1.36	10.43	K2O	0.14	0.12	0.05	0.04
Formula					H2O	3.73	3.71	3.65	3.95	H2O	10.58	10.41	10.35	10.41
#Si+4	3.028	2.8831	2.9144	2.9046	Total	97.76	97.64	92.68	99.33	Total	99.63	98.37	96.67	98.73
#Al+3	0.92	1.1822	1.0867	1.1182	Formula					Formula				
#Fe+3	0	0.0011	0.0044	0.0063	#Si IV	5.7313	5.1666	4.7201	6.3811	#Si IV	3.0838	2.8870	2.9505	2.8688
#Mg+2	0.001	0.0032	0.0013	0.0033	#Al IV	2.2687	2.8334	3.2799	1.6189	#Al IV	0.9162	1.1130	1.0495	1.1312
#Mn+2	0	0.0000	0.0007	0.0000	T site	8.0000	8.0000	8.0000	8.0000	T site	4.0000	4.0000	4.0000	4.0000
#Ca+2	0.051	0.0120	0.0794	0.0186	#Al VI	0.7528	0.6420	0.5672	1.5419	#Al VI	1.3338	1.2411	1.1402	1.2638
#Na+1	1.021	0.8743	0.8841	0.8782	#Ti VI	0.2326	0.3179	0.0562	0.1081	#Ti	0.0300	0.0132	0.0045	0.0062
#K+1	0.005	0.0132	0.0219	0.0859	#Fe +2	4.1559	4.6923	5.9374	3.0066	#Fe +2	4.0222	4.2958	4.4066	4.2882
#TOTAL	5.025	4.9690	4.9930	5.0152	#Mn +2	0.0683	0.0491	0.0648	0.0246	#Mn +2	0.0453	0.0467	0.0540	0.0564
#O-2	8	8.0000	8.0000	8.0000	#Mg	0.2379	0.3286	0.4564	0.2007	#Mg	0.2851	0.3097	0.3247	0.2944
Na+K+Ca	1.076	0.8995	0.9854	0.9828	O site	5.4475	6.0299	7.0821	4.8820	#Ca	0.0171	0.0050	0.0116	0.0088
ab	0.948	0.9720	0.8972	0.8937	#Ca	0.0247	0.0249	0.0343	0.0098	#Na	0.0353	0.0046	0.0093	0.0136
or	0.005	0.0147	0.0223	0.0874	#Na	0.0574	0.0546	0.0587	0.0415	#K	0.0203	0.0180	0.0077	0.0060
an	0.047	0.0133	0.0806	0.0190	#K	2.0488	1.3914	0.3088	2.0356	O site	5.7891	5.9340	5.9586	5.9373

Xca	0.047	0.01354	0.082	0.0208	A site	2.1309	1.4709	0.4018	2.0870	#O	10.0000	10.0000	10.0000	10.0000
					#O	20.0000	20.0000	20.0000	20.0000	#OH	8.0000	8.0000	8.0000	8.0000
					#OH	4.0000	4.0000	4.0000	4.0000	Charge	0.0000	0.0000	0.0000	0.0000
					Fe/Fe+Mg	0.9458	0.9345	0.9286	0.9374					

Table 2

Analyses/ Sa.No	SA9	SA11	SA12	SI-81C	SI-82B
SiO2	75.96	74.01	74.19	74.51	73.91
TiO2	0.08	0.16	0.08	0.05	0.12
Al2O3	13.23	14.06	14.27	14.20	13.88
Fe2O3tot	0.80	1.10	0.89	0.86	1.27
MnO	0.01	0.02	0.01	0.02	0.02
MgO	0.06	0.19	0.00	0.00	0.08
CaO	0.37	0.73	0.67	0.56	0.68
Na2O	4.21	3.77	4.47	4.45	4.31
K2O	4.63	5.05	4.90	4.68	5.02
P2O5	0.01	0.03	0.01	0.01	0.02
LOI	0.63	0.90	0.51	0.66	0.69
Total	100.00	100.00	100.00	100.00	100.00
Trace elments					
Ba	34.2	147.5	51.2	24.6	108.1
Ce	39.9	88.8	28.5	**nd**	67.3
Co	**nd**	**nd**	**nd**	**nd**	**nd**
Cr	26.7	38.5	20.0	30.2	25.3
La	30.0	42.1	28.6	11.2	43.3
Nb	9.5	22.4	19.9	13.3	15.4
Ni	17.2	27.7	23.1	19.0	14.8
Pb	29.3	15.9	24.4	10.5	16.9
Rb	141.0	178.9	282.9	135.2	200.4
Sr	6.3	29.1	14.3	13.9	17.5
Th	23.1	28.7	30.9	24.3	25.0
V	3.9	9.9	5.2	3.5	5.9

Y	27.0	57.0	72.1	47.8	51.8
Zn	62.1	35.1	13.6	33.0	37.1
Zr	95.4	171.7	100.4	135.7	123.0
Cu	13.0	4.7	3.1	4.9	4.2
Ga	13.0	15.0	14.8	13.9	13.9
Nd	**nd**	31.1	17.1	**nd**	30.4
S	351.3	**nd**	**nd**	**nd**	**nd**
Sc	2.9	7.1	5.3	2.7	4.4
CIPW Norm					
Q	33.14	31.28	28.2	29.77	28.33
or (KAS6)	27.56	30.14	29.13	27.87	29.9
ab (NAS6)	35.81	32.15	37.97	37.86	36.68
an (CAS2)	1.79	3.48	3.28	2.74	3.28
C(A)	0.63	1.12	0.4	0.81	0.15
Hy en(MS)	0.15	0.48	0	0	0.2
mt(FF)	0.03	0.07	0.03	0.07	0.07
he(F)	0.78	1.06	0.87	0.82	1.23
ap(CP)	0.02	0.07	0.02	0.02	0.04
Totals	99.92	99.84	99.92	99.95	99.88
Y/Nb	2.84	2.54	3.63	3.61	3.37
DI	96.51	93.57	95.3	95.5	94.91
T_{zircon} (ºC) Boehnke et al. (2013)	763	825	761	799	781
PQtz (Kb)	1.87	2.18	3.82	3	3.81
Emplacement depth (km)	5.1	5.9	10.3	8.1	10.3

Table 3

	Isotope ratios						Ages							Trace elements (ppm)		
Sample no/analysis	Pb207/Pb206	1s	Pb207/U235	1s	Pb206/U238	1s	Pb207/Pb206	1s	Pb207/U235	1s	Pb206/U238	1s	concordia	U	Th	Pb
SA12-17	0.06033	0.00168	0.83344	0.0136	0.10015	0.00128	615.4	59.06	615.5	7.53	615.3	7.52	100.03	300.55	133.85	38.28425
SA12-01	0.06059	0.00163	0.83873	0.01328	0.10041	0.0013	624.8	57.04	618.4	7.33	616.8	7.64	100.26	268.33	76.11	32.43958
SA12-14	0.0606	0.00177	0.83654	0.01563	0.10008	0.00131	625	61.89	617.2	8.64	614.9	7.68	100.37	196.49	67.54	24.25554
SA12-02	0.06061	0.00164	0.83287	0.01328	0.09967	0.0013	625.3	57.24	615.2	7.36	612.5	7.59	100.44	278.71	93.27	32.74589
SA12-21	0.06168	0.00169	0.79568	0.0122	0.09351	0.00118	663.2	57.76	594.4	6.9	576.3	6.98	103.14	475.21	245.06	57.9002
SA12-16	0.06164	0.00176	0.77899	0.01354	0.09162	0.00118	661.5	59.93	584.9	7.73	565.1	7	103.50	211.86	76.92	24.12298
SA12-20	0.06259	0.00173	0.81189	0.01273	0.09404	0.0012	694.3	57.81	603.5	7.13	579.4	7.04	104.16	342.18	125.37	40.29315
SA12-24	0.0627	0.00187	0.79295	0.01515	0.09169	0.00119	698	62.45	592.8	8.58	565.5	7.05	104.83	268.94	113.62	31.43153
SA12-15	0.06371	0.00179	0.81458	0.01362	0.09269	0.00119	732.1	58.34	605	7.62	571.4	7.05	105.88	230.43	97.85	26.87645
SA12-06	0.06528	0.00172	0.82984	0.01209	0.09219	0.00118	783.3	54.41	613.5	6.71	568.5	6.98	107.92	838.39	434.97	101.61871
SA12-25	0.06581	0.00197	0.80005	0.01513	0.08814	0.00114	800.5	61.45	596.9	8.53	544.5	6.78	109.62	244.11	101.9	27.48815
SA12-27	0.07422	0.00218	0.87399	0.01575	0.08539	0.0011	1047.4	58.2	637.7	8.53	528.2	6.55	120.73	336.81	193.18	0
SA12-11	0.08337	0.00216	1.08137	0.01444	0.09404	0.00119	1277.7	49.76	744.3	7.05	579.4	7.01	128.46	2966.31	1031.2	371.55147
SA12-07	0.08196	0.0023	0.83725	0.0144	0.07407	0.00097	1244.6	53.88	617.6	7.96	460.7	5.85	134.06	244.56	80.19	25.46841
SA12-26	0.07822	0.00208	0.55243	0.00733	0.05121	0.00063	1152.5	51.95	446.6	4.8	321.9	3.89	138.74	18900.25	11876	1559.065
SA12-10	0.08015	0.00206	0.61596	0.00808	0.05572	0.0007	1200.6	49.88	487.3	5.08	349.6	4.3	139.39	9583.69	6139.8	702.82089
SA12-09	0.0926	0.00248	0.65276	0.00978	0.05111	0.00066	1479.5	50.01	510.2	6.01	321.4	4.03	158.74	517.48	152.45	39.92071
SA12-08	0.10768	0.00296	0.6173	0.01001	0.04157	0.00054	1760.5	49.45	488.2	6.28	262.5	3.37	185.98	566.69	118.06	35.74394
SA12-13	0.11533	0.00303	0.68998	0.00949	0.04337	0.00055	1885	46.59	532.8	5.7	273.7	3.39	194.67	1236.53	415.54	70.3648
SA12-19	0.11824	0.00315	0.62841	0.00878	0.03853	0.00049	1929.9	46.99	495.1	5.48	243.7	3.01	203.16	1688.21	712.51	86.72271
SA12-22	0.13199	0.00349	0.82708	0.01113	0.04543	0.00057	2124.6	45.64	612	6.19	286.4	3.5	213.69	1679.43	579.24	130.57999
SA12-12	0.13631	0.00357	0.57532	0.00797	0.0306	0.00039	2180.8	44.93	461.5	5.14	194.3	2.44	237.52	955.42	281.42	93.15016
SA12-23	0.15889	0.00422	1.05931	0.01436	0.04833	0.00061	2443.9	44.28	733.5	7.08	304.3	3.72	241.05	782.3	258	70.92358
SA12-05	0.15937	0.00414	0.93444	0.01295	0.04252	0.00055	2449	43.27	670	6.8	268.4	3.38	249.63	2388.39	841.9	157.26246
SA12-18	0.13203	0.00352	0.32234	0.00452	0.0177	0.00022	2125.1	45.91	283.7	3.47	113.1	1.42	250.84	1560.52	277.14	42.28757
SA12-04	0.16395	0.0042	0.47305	0.00628	0.02093	0.00027	2496.8	42.46	393.3	4.33	133.5	1.69	294.61	6338.3	2630.9	223.70093
SA12-03	0.51702	0.01542	12.38403	0.24367	0.17373	0.00302	4290.5	43.15	2634	18.49	1032.6	16.6	255.08	953.4	2285.5	656.05192
SI82B-06	0.05914	0.00166	0.83039	0.01455	0.10179	0.00133	572.4	59.97	613.8	8.07	624.9	7.8	98.22	102.08	41.14	14.27945
SI82B-02	0.06133	0.0017	0.84428	0.01421	0.0998	0.0013	650.7	58.33	621.5	7.83	613.3	7.64	101.34	241.56	100.82	30.26442
SI82B-03	0.06143	0.00178	0.84937	0.01605	0.10025	0.00133	654.2	61.07	624.3	8.81	615.8	7.8	101.38	271.12	65.6	32.81564
SI82B-41	0.06097	0.00189	0.79869	0.01746	0.09502	0.00129	638.3	65.28	596.1	9.86	585.1	7.6	101.88	81.71	26.03	9.737765
SI82B-40	0.05916	0.00149	0.67984	0.00874	0.08336	0.00105	572.9	53.92	526.7	5.28	516.2	6.27	102.03	4427.91	2008.3	487.70761
SI82B-07	0.06207	0.00175	0.85838	0.01517	0.10026	0.00132	676.7	59.14	629.2	8.29	615.9	7.72	102.16	171.62	105.33	24.20551
SI82B-30	0.06135	0.00168	0.80999	0.01335	0.09576	0.00124	651.4	57.65	602.5	7.49	589.5	7.32	102.21	289.35	168.42	36.62902
SI82B-05	0.06041	0.00173	0.7526	0.01378	0.09032	0.00119	618.3	60.61	569.7	7.98	557.4	7.05	102.21	268.95	111.9	33.9813
SI82B-18	0.06065	0.00164	0.76655	0.01211	0.09164	0.00118	627	57.1	577.8	6.96	565.3	6.99	102.21	411.6	212	47.29682
SI82B-01	0.0621	0.00163	0.85215	0.0124	0.09947	0.00128	677.7	55.24	625.8	6.8	611.3	7.48	102.37	491.88	221.44	64.14449
SI82B-20	0.05997	0.00162	0.71417	0.01142	0.08636	0.00112	602.3	57.58	547.2	6.77	534	6.63	102.47	427.61	219.37	48.35359
SI82B-28	0.06054	0.00179	0.74396	0.01477	0.08913	0.00119	622.8	62.58	564.7	8.6	550.4	7.04	102.60	317.97	128.81	36.07591
SI82B-37	0.05922	0.00149	0.64592	0.00831	0.07911	0.001	575.2	53.93	506	5.12	490.8	5.97	103.10	5860.35	2493.3	586.12317
SI82B-04	0.06228	0.00167	0.82501	0.01269	0.09604	0.00124	683.7	56.17	610.8	7.06	591.1	7.29	103.33	337.76	187.46	42.76233
SI82B-14	0.06124	0.00165	0.73991	0.01164	0.08761	0.00113	647.7	56.86	562.4	6.79	541.4	6.71	103.88	281.04	124.67	32.60802
SI82B-24	0.05966	0.00152	0.55325	0.00731	0.06725	0.00085	591.4	54.29	447.1	4.78	419.5	5.15	106.58	7261.95	4127	567.6805
SI82B-08	0.06076	0.00155	0.58705	0.00769	0.07005	0.00089	630.9	53.96	469	4.92	436.4	5.36	107.47	4990.33	2766.8	431.64109
SI82B-42	0.06315	0.00321	0.71514	0.03229	0.08215	0.00144	713.3	104.45	547.8	19.11	508.9	8.56	107.64	43.02	18.66	5.591991

SI82B-29	0.06341	0.00183	0.70636	0.01318	0.08079	0.00107	722.2	59.92	542.6	7.84	500.8	6.37	108.35	179.68	60.66	18.55102
SI82B-15	0.06383	0.00178	0.71747	0.01239	0.0815	0.00107	736.1	58.03	549.2	7.33	505.1	6.36	108.73	265.91	117.77	31.11474
SI82B-19	0.06812	0.00188	0.83327	0.01403	0.08871	0.00116	872.1	56.21	615.4	7.77	547.9	6.86	112.32	317.06	141.6	31.69701
SI82B-17	0.0816	0.00207	1.505	0.01945	0.13374	0.0017	1236	48.77	932.4	7.88	809.2	9.64	115.22	8084.15	3275.2	1510.3178
SI82B-33	0.06817	0.0018	0.57239	0.00857	0.0609	0.00078	873.6	53.82	459.6	5.53	381.1	4.75	120.60	357.56	122.5	31.4812
SI82B-16	0.06341	0.00161	0.32834	0.0043	0.03755	0.00048	722	53.07	288.3	3.28	237.6	2.96	121.34	6881.72	3781.6	349.90124
SI82B-26	0.07835	0.00232	0.92484	0.01828	0.08561	0.00116	1155.7	57.6	664.9	9.64	529.5	6.87	125.57	232.28	101.04	27.20745
SI82B-38	0.06261	0.00159	0.19193	0.0025	0.02224	0.00028	694.9	53.08	178.3	2.13	141.8	1.77	125.74	10241.36	5459.4	312.31043
SI82B-10	0.06929	0.00179	0.44509	0.00616	0.04657	0.00059	907.5	52.43	373.8	4.33	293.4	3.66	127.40	4761.1	2396.1	533.26665
SI82B-35	0.07015	0.00178	0.46075	0.00598	0.04764	0.0006	932.7	51.08	384.8	4.15	300	3.71	128.27	5017.6	2285.6	314.71074
SI82B-23	0.07937	0.00209	0.78637	0.01158	0.07185	0.00092	1181.4	51.21	589.1	6.58	447.3	5.56	131.70	848.73	332.75	82.79793
SI82B-27	0.08258	0.00262	0.79564	0.01806	0.06988	0.00098	1259.2	60.77	594.4	10.21	435.4	5.89	136.52	256.69	101.09	24.59385
SI82B-31	0.08083	0.00212	0.66213	0.00967	0.05941	0.00076	1217.3	50.75	515.9	5.91	372.1	4.64	138.65	462.51	160.85	32.88295
SI82B-11	0.08548	0.00224	0.70314	0.01006	0.05964	0.00077	1326.4	49.88	540.7	6	373.4	4.66	144.80	1262.51	460.38	102.33639
SI82B-12	0.08004	0.00206	0.39934	0.00543	0.03618	0.00046	1197.9	49.95	341.2	3.94	229.1	2.87	148.93	4540.2	2040.1	219.76654
SI82B-22	0.08009	0.00205	0.17632	0.00236	0.01596	0.0002	1199.3	49.66	164.9	2.04	102.1	1.29	161.51	7438.31	4033	177.179
SI82B-25	0.10582	0.003	0.51472	0.00916	0.03527	0.00047	1728.7	51.1	421.6	6.14	223.5	2.93	188.64	1264.67	295.2	56.11481
SI82B-39	0.10246	0.00263	0.20315	0.00276	0.01438	0.00018	1669.1	46.67	187.8	2.33	92.1	1.16	203.91	4844.93	3364.4	101.58078
SI82B-13	0.11541	0.00297	0.12099	0.00164	0.0076	0.0001	1886.3	45.6	116	1.48	48.8	0.62	237.70	4940.4	2168.4	98.27695
SI82B-09	0.13513	0.00379	0.45207	0.00776	0.02426	0.00032	2165.7	48.11	378.7	5.43	154.5	2.04	245.11	2519.96	779.66	94.35143
SI82B-32	0.17627	0.00446	0.30824	0.00398	0.01268	0.00016	2618	41.49	272.8	3.09	81.2	1.02	335.96	8412	6066.4	291.92468
SI82B-34	0.1779	0.00468	0.24073	0.0035	0.00981	0.00013	2633.4	43.06	219	2.87	63	0.81	347.62	4768.6	1951.6	84.38777
SI82B-21	0.18757	0.00484	0.25792	0.00353	0.00997	0.00013	2721	41.89	233	2.85	64	0.82	364.06	7166.7	4694.5	130.30083
SI82B-36	0.3327	0.00849	0.3035	0.00402	0.00662	0.00008	3629.6	38.53	269.1	3.13	42.5	0.54	633.18	12103.41	22042	195.67743
SA9-02	0.05949	0.00103	0.7939	0.01164	0.09675	0.00061	585.2	37.17	593.4	6.59	595.4	3.56	99.66	91.84	48.31	11.85579
SA9-40	0.05997	0.00063	0.80208	0.00454	0.09697	0.00049	602.5	22.67	598	2.56	596.6	2.91	100.23	7577.76	4457.7	876.62062
SA9-41	0.0603	0.00065	0.80134	0.00491	0.09635	0.0005	614.4	23.2	597.6	2.77	593	2.91	100.78	3763.33	1246.8	445.84629
SA9-35	0.06082	0.00076	0.8179	0.00702	0.09751	0.00053	632.7	26.54	606.9	3.92	599.8	3.1	101.18	400.22	154.82	48.6725
SA9-29	0.06085	0.00064	0.81925	0.00449	0.09762	0.0005	634	22.34	607.6	2.5	600.4	2.92	101.20	7030.09	3535.8	887.42124
SA9-04	0.06142	0.00064	0.82695	0.00458	0.09763	0.0005	653.8	22.33	611.9	2.54	600.5	2.92	101.90	4794.36	1927.9	602.03015
SA9-13	0.06148	0.00131	0.80924	0.01536	0.09543	0.00068	656.2	44.91	602	8.62	587.6	4.02	102.45	76.79	39.6	9.42043
SA9-36	0.06173	0.00077	0.82218	0.00718	0.09657	0.00053	664.9	26.62	609.3	4	594.3	3.09	102.52	477.69	187.84	57.98121
SA9-14	0.06201	0.00101	0.8239	0.01109	0.09633	0.00059	674.6	34.48	610.2	6.17	592.9	3.48	102.92	90.52	31.86	11.315813
SA9-20	0.06234	0.00068	0.83454	0.00515	0.09706	0.0005	685.8	22.98	616.1	2.85	597.2	2.94	103.16	5823.31	2298.7	707.39295
SA9-37	0.06322	0.00096	0.83578	0.01022	0.09586	0.00057	715.5	32.09	616.8	5.65	590.1	3.36	104.52	207.98	107.13	25.81619
SA9-38	0.06413	0.00092	0.84045	0.00925	0.09502	0.00055	746	29.89	619.4	5.11	585.2	3.23	105.84	259.55	92.45	29.56847
SA9-15	0.06536	0.00086	0.87497	0.00832	0.09707	0.00054	785.9	27.29	638.3	4.5	597.2	3.18	106.88	558.84	217.07	70.0979
SA9-06	0.06657	0.00084	0.89153	0.00795	0.0971	0.00053	824.4	26.22	647.2	4.27	597.4	3.13	108.34	285.49	96.94	36.68402
SA9-05	0.05864	0.00061	1.05861	0.00567	0.13089	0.00066	553.8	22.49	733.1	2.79	793	3.79	92.45	9135.83	2348	3412.0414
SA9-22	0.06816	0.00073	0.88613	0.00523	0.09426	0.00048	873.5	21.98	644.3	2.82	580.7	2.85	110.95	4137	1996.1	511.72532
SA9-28	0.07031	0.00073	0.99248	0.00536	0.10234	0.00052	937.5	21.2	700	2.73	628.1	3.04	111.45	7236.9	3366.4	1000.6603
SA9-31	0.07241	0.00118	0.9174	0.01229	0.09187	0.00058	997.4	32.73	661	6.51	566.6	3.42	116.66	551.39	260.89	60.45266
SA9-25	0.07447	0.00078	1.0029	0.00555	0.09765	0.0005	1053.9	21.29	705.3	2.81	600.6	2.92	117.43	5306.7	2155.7	682.34896
SA9-16	0.08773	0.00096	1.03793	0.00658	0.08578	0.00045	1376.6	20.9	722.9	3.28	530.5	2.65	136.27	502.37	233.7	81.28168
SA9-21	0.09684	0.00105	1.25609	0.00763	0.09405	0.00049	1564.1	20.1	826.1	3.43	579.4	2.87	142.58	2363.02	1064.4	326.26654
SA9-30	0.09286	0.00124	1.01793	0.00993	0.07948	0.00046	1485	25.22	712.9	5	493	2.74	144.60	472.21	177.56	56.68825
SA9-17	0.09438	0.00099	1.04226	0.00577	0.08007	0.00041	1515.7	19.65	725	2.87	496.6	2.44	145.99	6552.35	3360.7	636.63802
SA9-32	0.10068	0.00105	1.25999	0.00692	0.09074	0.00046	1636.7	19.3	827.9	3.11	559.9	2.74	147.87	4380.68	2514.9	570.93718
SA9-34	0.10582	0.00111	1.1265	0.00631	0.07719	0.00039	1728.6	19.19	766.1	3.01	479.3	2.36	159.84	3692.98	1662.7	436.7269
SA9-12	0.1056	0.0011	1.09049	0.00591	0.07487	0.00038	1724.8	19.02	748.7	2.87	465.5	2.29	160.84	7557.78	4682	902.65488

SA9-27	0.09005	0.00097	0.47731	0.00287	0.03843	0.0002	1426.4	20.4	396.2	1.97	243.1	1.23	162.98	8017.16	5090.7	415.03896
SA9-08	0.11932	0.00125	0.86363	0.00478	0.05248	0.00027	1946.1	18.63	632.1	2.6	329.7	1.64	191.72	9520.21	5165.1	740.86299
SA9-07	0.13551	0.00141	1.33099	0.00721	0.07122	0.00036	2170.6	18.06	859.3	3.14	443.5	2.18	193.75	6943.99	3428.1	767.0156
SA9-18	0.12903	0.00135	1.10961	0.00614	0.06236	0.00032	2084.7	18.33	758	2.95	389.9	1.93	194.41	4815.35	2323.5	465.13481
SA9-42	0.12378	0.00138	0.90799	0.00601	0.05319	0.00028	2011.3	19.68	656	3.2	334.1	1.72	196.35	631.74	213.01	73.50529
SA9-10	0.13174	0.00138	1.0443	0.0057	0.05748	0.00029	2121.3	18.19	726.1	2.83	360.3	1.79	201.53	6969.89	2845.5	667.45741
SA9-23	0.13235	0.00149	0.42512	0.00285	0.02329	0.00012	2129.3	19.52	359.7	2.03	148.4	0.78	242.39	20782.19	7077.1	820.53801
SA9-03	0.30192	0.00314	4.11159	0.02197	0.09874	0.0005	3480.1	15.98	1656.6	4.36	607	2.96	272.92	8209.99	4623.7	1790.9336
SA9-26	0.16994	0.00189	0.57446	0.00376	0.02451	0.00013	2557.1	18.53	460.9	2.42	156.1	0.82	295.26	1187.06	751.2	46.57581
SA9-11	0.20554	0.00215	0.96678	0.00527	0.0341	0.00017	2870.7	16.89	686.8	2.72	216.2	1.09	317.67	6681.4	2941.3	427.71856
SA9-01	0.19948	0.00209	0.41763	0.00229	0.01518	0.00008	2822	17	354.4	1.64	97.1	0.49	364.98	23409.1	10609	645.04753
SA9-19	0.22318	0.00243	0.4661	0.00286	0.01514	0.00008	3003.8	17.41	388.5	1.98	96.9	0.51	400.93	9819.32	5359.8	288.64105
SA9-09	0.26735	0.00291	0.59326	0.00361	0.01609	0.00009	3290.5	16.98	472.9	2.3	102.9	0.54	459.57	2690.2	3168.9	89.76751
SA9-39	0.29097	0.00305	0.76277	0.00417	0.01901	0.0001	3422.8	16.18	575.6	2.4	121.4	0.62	474.14	8314.5	4074.3	342.02385
SA9-24	0.53402	0.00561	2.59025	0.0142	0.03517	0.00018	4338	15.31	1297.9	4.02	222.8	1.14	582.54	2823.17	1016.4	302.95946
SA9-33	0.35551	0.00379	0.44656	0.00256	0.00911	0.00005	3730.8	16.13	374.9	1.8	58.4	0.31	641.95	6655.75	3177.1	146.9439
SA11-37	0.36946	0.00978	0.12797	0.00186	0.00251	0.00003	3789.2	39.55	122.3	1.68	16.1	0.22	759.63	26687.77	2549.5	778.8077
SA11-33	0.38153	0.01037	0.13643	0.00211	0.00259	0.00004	3837.8	40.46	129.9	1.88	16.7	0.23	777.84	11537.71	7734.7	78.58061
SA11-16	0.27109	0.00731	0.18753	0.00286	0.00501	0.00007	3312.3	41.66	174.5	2.45	32.2	0.43	541.93	6824.82	6354.2	88.42098
SA11-20	0.35275	0.0092	0.26293	0.00366	0.0054	0.00007	3718.9	39.12	237	2.94	34.7	0.46	683.00	7617.09	3381.1	99.41131
SA11-07	0.16016	0.00453	0.23774	0.00411	0.01076	0.00015	2457.4	47	216.6	3.37	69	0.93	313.91	315.68	151.14	35.30246
SA11-36	0.23509	0.00606	0.35599	0.00484	0.01097	0.00014	3087	40.52	309.2	3.62	70.3	0.91	439.83	7557.87	1805	157.12516
SA11-27	0.29793	0.00773	0.45951	0.00635	0.01117	0.00015	3459.5	39.66	383.9	4.42	71.6	0.93	536.17	3724.23	2601.9	92.28312
SA11-17	0.22127	0.00569	0.40164	0.0054	0.01316	0.00017	2989.9	40.79	342.8	3.91	84.3	1.08	406.64	5289.84	3556.1	129.14317
SA11-04	0.29278	0.00753	0.55135	0.00738	0.01365	0.00018	3432.4	39.41	445.9	4.83	87.4	1.12	510.18	3665.51	3551.1	111.17535
SA11-03	0.15447	0.00395	0.54935	0.00723	0.02579	0.00033	2396	42.86	444.6	4.74	164.1	2.07	270.93	7470.79	2821	324.0153
SA11-09	0.20717	0.0054	0.7506	0.01048	0.02627	0.00034	2883.5	41.7	568.6	6.08	167.1	2.14	340.28	2406.81	1169.3	113.96004
SA11-05	0.13696	0.00361	0.54868	0.00793	0.02905	0.00038	2189.2	45.08	444.1	5.2	184.6	2.36	240.57	1477.09	2224.9	67.07065
SA11-21	0.14113	0.00367	0.63528	0.00888	0.03262	0.00042	2241.1	44.3	499.4	5.51	206.9	2.65	241.37	2476.67	1128.2	125.44785
SA11-12	0.14096	0.00367	0.8402	0.01174	0.04321	0.00056	2239	44.33	619.3	6.48	272.7	3.46	227.10	1473.18	296.51	96.36007
SA11-08	0.08346	0.0023	0.49826	0.00825	0.04328	0.00057	1279.7	52.96	410.5	5.59	273.1	3.52	150.31	850.33	315.68	49.04091
SA11-41	0.15746	0.00416	0.98694	0.01449	0.04539	0.0006	2428.6	44.09	697.2	7.41	286.1	3.72	243.69	1128.13	341.41	81.98192
SA11-13	0.09522	0.0025	0.8128	0.01163	0.06187	0.0008	1532.5	48.54	604	6.52	387	4.87	156.07	833.69	257.57	69.76838
SA11-24	0.06889	0.00209	0.69685	0.01445	0.0733	0.001	895.5	61.4	536.9	8.65	456	6.04	117.74	187.5	48.03	18.79424
SA11-18	0.07171	0.00204	0.73318	0.01319	0.0741	0.00099	977.7	56.94	558.4	7.73	460.8	5.94	121.18	320.9	109.85	29.56267
SA11-38	0.12327	0.00331	1.28329	0.01976	0.07539	0.00101	2004	46.86	838.3	8.79	468.6	6.04	178.89	193.17	45.56	20.71538
SA11-34	0.07047	0.00195	0.76696	0.01289	0.07883	0.00105	942	55.67	578	7.41	489.2	6.29	118.15	423.48	137.28	41.12302
SA11-15	0.05985	0.00158	0.82736	0.01227	0.1002	0.0013	598.1	56.33	612.1	6.82	615.6	7.62	99.43	385.43	136.35	46.77265
SA11-01	0.0601	0.00167	0.82715	0.01406	0.0998	0.00131	607	59.02	612	7.81	613.3	7.66	99.79	277.09	119.82	34.67224
SA11-31	0.06098	0.00164	0.83573	0.01294	0.09928	0.00131	638.5	56.7	616.8	7.16	610.2	7.67	101.08	321.94	128.1	40.87294
SA11-40	0.06106	0.0017	0.81898	0.01413	0.09713	0.0013	641.3	58.9	607.5	7.89	597.5	7.65	101.67	212.49	69.8	23.85447
SA11-32	0.06147	0.00169	0.83191	0.01378	0.09803	0.0013	655.8	57.9	614.7	7.64	602.9	7.64	101.96	275.68	101.09	32.72934
SA11-02	0.06112	0.0018	0.7918	0.01534	0.09393	0.00125	643.6	61.92	592.2	8.69	578.7	7.39	102.33	172.05	56.45	24.70048
SA11-25	0.06153	0.00177	0.80885	0.01488	0.09524	0.00128	657.9	60.35	601.8	8.35	586.5	7.53	102.61	259.32	131.52	30.0001
SA11-39	0.06159	0.00158	0.80722	0.01094	0.09491	0.00124	660	54.18	600.9	6.15	584.5	7.3	102.81	5238.98	2141.2	672.94715
SA11-10	0.06191	0.00167	0.81053	0.01266	0.09491	0.00124	671	56.64	602.8	7.1	584.5	7.28	103.13	294.89	140.28	35.07499
SA11-35	0.06204	0.00178	0.79889	0.0147	0.09327	0.00126	675.4	60.16	596.2	8.3	574.8	7.42	103.72	497.07	213.49	42.77153
SA11-26	0.06198	0.00162	0.78699	0.01118	0.092	0.0012	673.2	54.86	589.5	6.35	567.4	7.07	103.89	1886.51	638.38	208.9699
SA11-29	0.0623	0.00203	0.75367	0.01796	0.08764	0.00123	684.3	68.05	570.3	10.4	541.6	7.31	105.30	126.15	37.54	13.689818
SA11-23	0.06288	0.00162	0.78032	0.01059	0.08992	0.00116	704.3	53.88	585.7	6.04	555	6.88	105.53	4908.72	2193.4	548.10133

SA11-14	0.06275	0.00167	0.76625	0.01163	0.08851	0.00115	699.8	55.83	577.6	6.69	546.7	6.82	105.65	420.09	130.95	45.06183
SA11-19	0.06271	0.00185	0.71832	0.01404	0.08302	0.00112	698.3	61.6	549.7	8.3	514.1	6.67	106.92	332.09	163.23	36.03136
SA11-22	0.06395	0.00166	0.78197	0.01089	0.0886	0.00115	740.1	53.97	586.6	6.2	547.3	6.8	107.18	2048.55	616.48	227.42174
SA11-28	0.06453	0.0017	0.74936	0.01104	0.08413	0.0011	758.9	54.72	567.9	6.41	520.7	6.54	109.06	1920.39	767.19	199.11695
SA11-11	0.06594	0.00184	0.75437	0.01287	0.08294	0.00109	804.3	57.26	570.8	7.45	513.6	6.5	111.14	203.46	94.7	23.41153
SA11-06	0.06699	0.00184	0.74714	0.0122	0.08086	0.00106	837.4	56.07	566.6	7.09	501.3	6.3	113.03	426.79	364.32	45.77276
SA11-30	0.0679	0.00192	0.79648	0.0142	0.08498	0.00114	865.5	57.66	594.8	8.03	525.8	6.78	113.12	334.6	139.51	35.20597
SI81C-32	0.05661	0.00144	0.91406	0.01213	0.11705	0.00151	475.8	55.46	659.2	6.43	713.6	8.74	92.38	7202.37	3798.5	1034.1495
SI81C-29	0.05545	0.0014	0.78502	0.01032	0.10264	0.00133	430	55.08	588.3	5.87	629.9	7.76	93.40	12232.39	5409.3	1938.7108
SI81C-42	0.05698	0.00144	0.84949	0.01116	0.10809	0.0014	490.2	55.51	624.4	6.13	661.6	8.13	94.38	9710.23	3621.8	1289.3813
SI81C-08	0.06304	0.0016	1.16539	0.01537	0.13404	0.00173	709.4	52.99	784.5	7.21	810.9	9.85	96.74	9198.92	2925.4	1717.9832
SI81C-02	0.06163	0.00156	0.93051	0.01227	0.10946	0.00142	661.3	53.4	667.9	6.45	669.6	8.23	99.75	5536.28	2127	738.55891
SI81C-41	0.05951	0.00151	0.79101	0.01058	0.09637	0.00125	585.8	54.29	591.7	6	593.1	7.34	99.76	7533.81	4903.9	933.56098
SI81C-34	0.06109	0.00156	0.83054	0.01114	0.09856	0.00128	642.5	53.83	613.9	6.18	606	7.49	101.30	5002.13	2391.3	611.58377
SI81C-37	0.06545	0.0017	1.09124	0.01564	0.12088	0.00158	788.8	53.6	749.1	7.59	735.6	9.07	101.84	589.47	94.31	80.56632
SI81C-18	0.05984	0.00152	0.71754	0.00947	0.08693	0.00112	597.9	53.97	549.2	5.6	537.3	6.67	102.21	6870.94	2735.7	727.89711
SI81C-15	0.06111	0.00155	0.77188	0.01027	0.09157	0.00119	643.3	53.7	580.8	5.89	564.8	7	102.83	6467.69	3129.3	740.84102
SI81C-36	0.06701	0.00174	1.10629	0.01573	0.11969	0.00156	838.1	53.06	756.4	7.58	728.8	8.98	103.79	403.24	71.71	69.68475
SI81C-16	0.06791	0.00194	0.96832	0.01788	0.10337	0.0014	865.9	58.14	687.6	9.22	634.1	8.16	108.44	258.91	183.01	39.15046
SI81C-40	0.08166	0.00207	1.55112	0.02038	0.13772	0.00178	1237.3	48.72	950.9	8.11	831.8	10.09	114.32	6036	2285.3	1127.616
SI81C-10	0.06332	0.00161	0.44032	0.00592	0.05042	0.00065	718.8	53.19	370.5	4.17	317.1	4.01	116.84	8555.25	4054.7	557.83279
SI81C-21	0.0731	0.00186	0.93665	0.01242	0.09289	0.0012	1016.9	50.59	671.1	6.51	572.6	7.09	117.20	6891.32	3610.6	836.96512
SI81C-28	0.08584	0.00217	1.45892	0.01921	0.12322	0.00159	1334.5	48.27	913.6	7.93	749.1	9.15	121.96	7046.99	2872.3	1148.8799
SI81C-06	0.07854	0.00199	0.60779	0.00801	0.05611	0.00073	1160.5	49.44	482.2	5.06	351.9	4.43	137.03	9326.04	2818.2	907.39931
SI81C-14	0.1287	0.00412	1.52433	0.03503	0.08587	0.00128	2080.3	55.29	940.2	14.09	531	7.63	177.06	95.17	560.25	26.08647
SI81C-35	0.09407	0.00241	0.23927	0.00326	0.01844	0.00024	1509.6	47.58	217.8	2.67	117.8	1.51	184.89	8066.89	8996.2	229.91774
SI81C-05	0.09945	0.00253	0.31137	0.00416	0.0227	0.00029	1613.7	46.68	275.2	3.22	144.7	1.85	190.19	6645.26	2678	257.63628
SI81C-11	0.19846	0.00511	0.06998	0.00097	0.00256	0.00003	2813.6	41.45	68.7	0.92	16.5	0.21	416.36	24166.54	19520	117.91662
SI81C-09	0.24793	0.0063	0.66366	0.00882	0.01941	0.00025	3171.6	39.73	516.9	5.39	123.9	1.59	417.19	6534.2	4036.7	251.65245
SI81C-39	0.25073	0.00638	0.30301	0.00404	0.00876	0.00011	3189.4	39.71	268.7	3.15	56.2	0.73	478.11	17323.95	15717	306.20976
SI81C-22	0.3292	0.00843	0.60985	0.00826	0.01343	0.00018	3613.4	38.71	483.5	5.21	86	1.12	562.21	4924.16	2895.7	151.77277
SI81C-03	0.32582	0.00828	0.46813	0.00621	0.01042	0.00014	3597.5	38.47	389.9	4.29	66.8	0.86	583.68	7599.66	4320.7	179.58992
SI81C-17	0.31783	0.0081	0.39584	0.0053	0.00903	0.00012	3559.4	38.7	338.6	3.85	57.9	0.75	584.80	9596.94	6075.5	194.68208
SI81C-19	0.35257	0.00899	0.4985	0.00667	0.01025	0.00013	3718.1	38.28	410.7	4.52	65.7	0.85	625.11	5225.44	2984.8	199.39386
SI81C-13	0.33525	0.00854	0.35794	0.00478	0.00774	0.0001	3641.3	38.45	310.7	3.57	49.7	0.64	625.15	8382.76	3857.3	149.34069
SI81C-01	0.35086	0.00898	0.47537	0.00643	0.00982	0.00013	3710.7	38.45	394.9	4.42	63	0.82	626.83	7969.07	5087.4	186.58919
SI81C-26	0.36582	0.0093	0.56429	0.00748	0.01118	0.00015	3774.2	38.02	454.3	4.86	71.7	0.93	633.61	5543.05	3050	152.06179
SI81C-30	0.38745	0.00982	0.60934	0.00802	0.0114	0.00015	3861.1	37.71	483.1	5.06	73.1	0.94	660.88	11577.48	3121.4	322.30444
SI81C-04	0.36615	0.00954	0.42812	0.00607	0.00848	0.00011	3775.5	38.97	361.8	4.31	54.4	0.72	665.07	5345.12	2468.5	110.5912
SI81C-07	0.38881	0.01001	0.57843	0.00793	0.01079	0.00014	3866.4	38.26	463.5	5.1	69.2	0.91	669.80	5210.62	4944.4	145.67375
SI81C-23	0.37227	0.00948	0.43422	0.00578	0.00846	0.00011	3800.7	38.01	366.2	4.09	54.3	0.7	674.40	5923.5	4273.9	126.41452
SI81C-31	0.36232	0.0092	0.36197	0.00479	0.00724	0.00009	3759.6	38.04	313.7	3.57	46.5	0.6	674.62	11238.16	13281	204.22893
SI81C-33	0.3667	0.00937	0.38669	0.0052	0.00765	0.0001	3777.8	38.21	331.9	3.81	49.1	0.64	675.97	6517.96	4960.3	123.32565
SI81C-24	0.41983	0.01067	0.75821	0.01006	0.01309	0.00017	3981.7	37.53	573	5.81	83.9	1.08	682.96	6719.79	5412.9	234.01334
SI81C-12	0.41894	0.01071	0.56024	0.00754	0.0097	0.00013	3978.5	37.74	451.7	4.9	62.2	0.81	726.21	6527.46	3617.5	168.23138
SI81C-20	0.4256	0.01091	0.52454	0.0071	0.00894	0.00012	4002.1	37.78	428.2	4.73	57.3	0.75	747.29	5091.54	3455.6	124.20296
SI81C-38	0.45389	0.0117	0.60181	0.00826	0.00961	0.00013	4098	37.77	478.4	5.24	61.7	0.81	775.36	6158.15	4723.8	167.84128
SI81C-25	0.43573	0.01105	0.4466	0.00588	0.00743	0.0001	4037.2	37.31	374.9	4.13	47.7	0.62	785.95	14728.41	9054.2	295.05649
SI81C-27	0.55483	0.01406	0.98949	0.013	0.01293	0.00017	4393.9	36.54	698.5	6.64	82.8	1.07	843.60	9722.43	5062.3	393.99348

figure

Click here to access/download;figure;Figures.docx

Figure 1

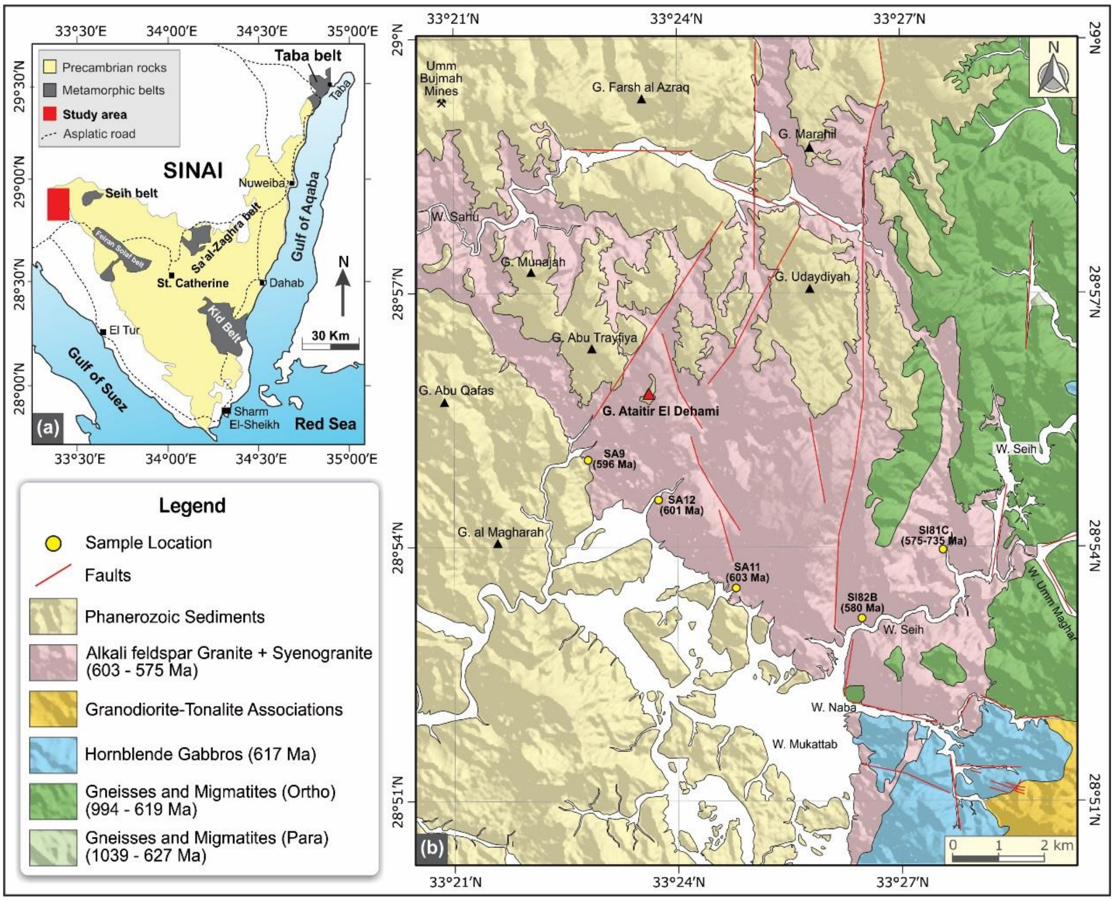

Figure 2

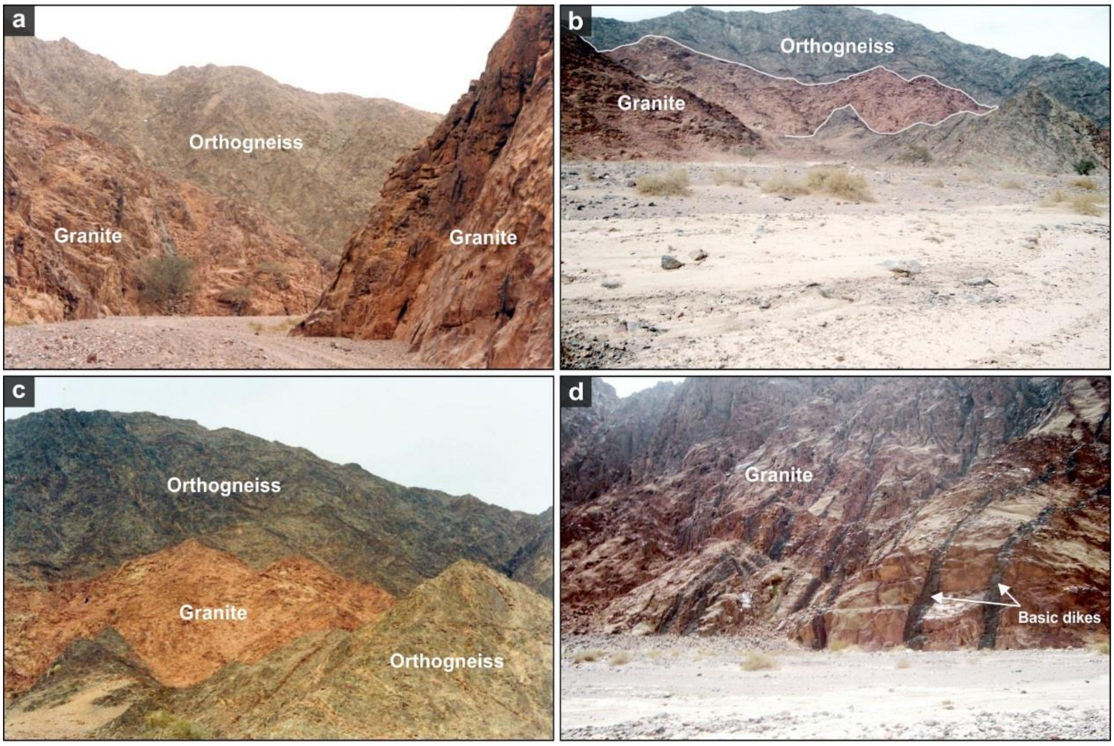
a
Orthogneiss
Granite
Granite
b
Orthogneiss
Granite
c
Orthogneiss
Granite
Orthogneiss
d
Granite
Basic dikes

Figure 3

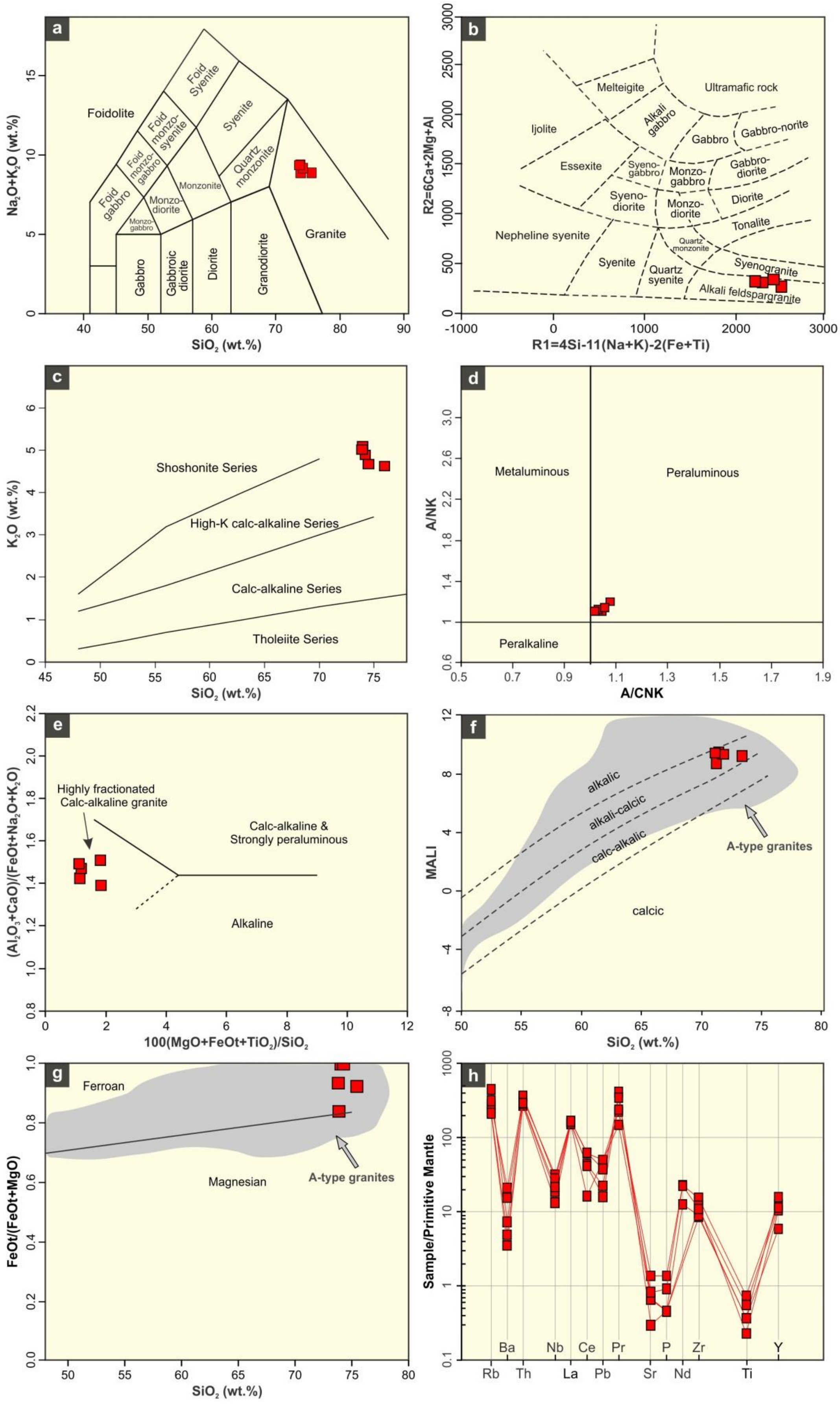

a
Foidolite
Foid Syenite
Syenite
Foid monzo-syenite
Foid monzo-gabbro
Foid gabbro
Monzonite
Quartz monzonite
Monzo-diorite
Monzo-gabbro
Gabbro
Gabbroic diorite
Diorite
Granodiorite
Granite
Na_2O+K_2O (wt.%)
SiO_2 (wt.%)
b
Melteigite
Ultramafic rock
Ijolite
Alkali gabbro
Gabbro
Gabbro-norite
Essexite
Syeno-gabbro
Monzo-gabbro
Gabbro-diorite
Syeno-diorite
Monzo-diorite
Diorite
Nepheline syenite
Quartz monzonite
Tonalite
Syenite
Quartz syenite
Syenogranite
Alkali feldspargranite
R2=6Ca+2Mg+Al
R1=4Si-11(Na+K)-2(Fe+Ti)
c
Shoshonite Series
High-K calc-alkaline Series
Calc-alkaline Series
Tholeiite Series
K_2O (wt.%)
SiO_2 (wt.%)
d
Metaluminous
Peraluminous
Peralkaline
A/NK
A/CNK
e
Highly fractionated Calc-alkaline granite
Calc-alkaline & Strongly peraluminous
Alkaline
$(Al_2O_3+CaO)/(FeOt+Na_2O+K_2O)$
$100(MgO+FeOt+TiO_2)/SiO_2$
f
alkalic
alkali-calcic
calc-alkalic
calcic
A-type granites
MALI
SiO_2 (wt.%)
g
Ferroan
Magnesian
A-type granites
FeOt/(FeOt+MgO)
SiO_2 (wt.%)
h
Sample/Primitive Mantle
Rb Ba Th Nb La Ce Pb Pr Sr P Nd Zr Ti Y

Figure 4

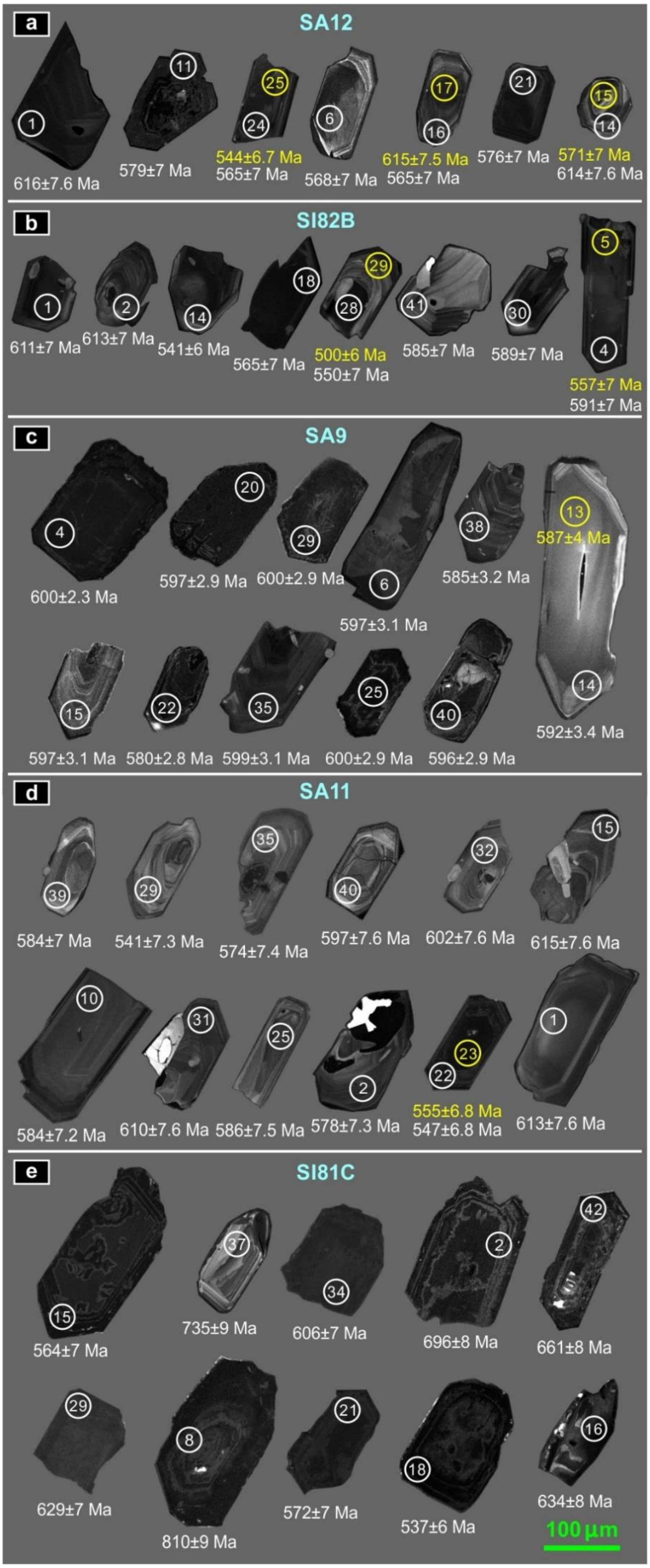
a
SA12
616±7.6 Ma
579±7 Ma
544±6.7 Ma
565±7 Ma
568±7 Ma
615±7.5 Ma
565±7 Ma
576±7 Ma
571±7 Ma
614±7.6 Ma
b
SI82B
611±7 Ma
613±7 Ma
541±6 Ma
565±7 Ma
500±6 Ma
550±7 Ma
585±7 Ma
589±7 Ma
557±7 Ma
591±7 Ma
c
SA9
600±2.3 Ma
597±2.9 Ma
600±2.9 Ma
597±3.1 Ma
585±3.2 Ma
587±4 Ma
592±3.4 Ma
597±3.1 Ma
580±2.8 Ma
599±3.1 Ma
600±2.9 Ma
596±2.9 Ma
d
SA11
584±7 Ma
541±7.3 Ma
574±7.4 Ma
597±7.6 Ma
602±7.6 Ma
615±7.6 Ma
584±7.2 Ma
610±7.6 Ma
586±7.5 Ma
578±7.3 Ma
555±6.8 Ma
547±6.8 Ma
613±7.6 Ma
e
SI81C
564±7 Ma
735±9 Ma
606±7 Ma
696±8 Ma
661±8 Ma
629±7 Ma
810±9 Ma
572±7 Ma
537±6 Ma
634±8 Ma
100 µm

Figure 5

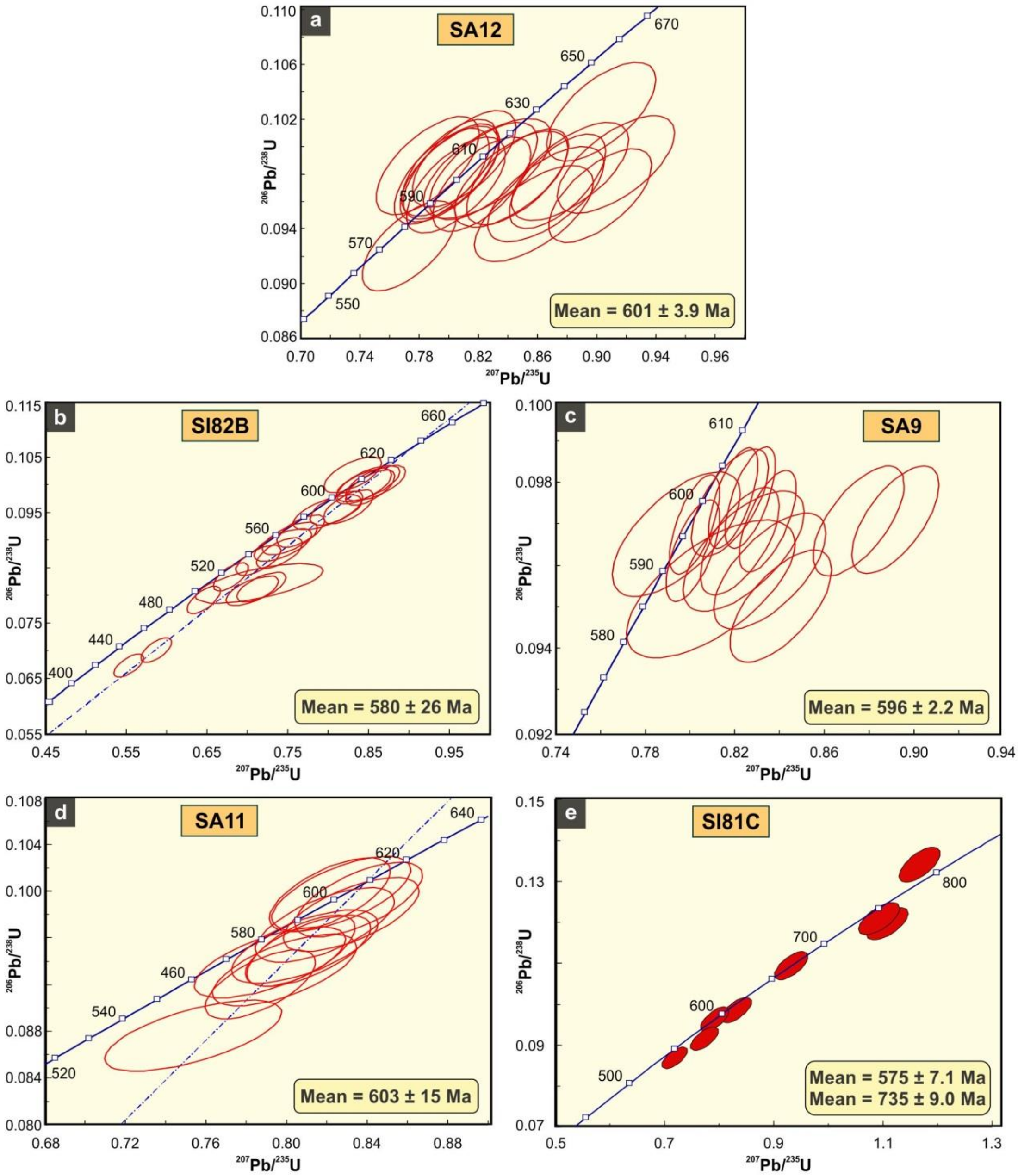

a
SA12
Mean = 601 ± 3.9 Ma
670
650
630
610
590
570
550
0.110
0.106
0.102
0.094
0.090
0.086
0.70
0.74
0.78
0.82
0.86
0.90
0.94
0.96
206Pb/238U
207Pb/235U
b
SI82B
Mean = 580 ± 26 Ma
660
620
600
560
520
480
440
400
0.115
0.105
0.095
0.075
0.065
0.055
0.45
0.55
0.65
0.75
0.85
0.95
206Pb/238U
207Pb/235U
c
SA9
Mean = 596 ± 2.2 Ma
610
600
590
580
0.100
0.098
0.094
0.092
0.74
0.78
0.82
0.86
0.90
0.94
206Pb/238U
207Pb/235U
d
SA11
Mean = 603 ± 15 Ma
640
620
600
580
460
540
520
0.108
0.104
0.100
0.088
0.084
0.080
0.68
0.72
0.76
0.80
0.84
0.88
206Pb/238U
207Pb/235U
e
SI81C
Mean = 575 ± 7.1 Ma
Mean = 735 ± 9.0 Ma
800
700
600
500
0.15
0.13
0.09
0.07
0.5
0.7
0.9
1.1
1.3
206Pb/238U
207Pb/235U

Figure 6

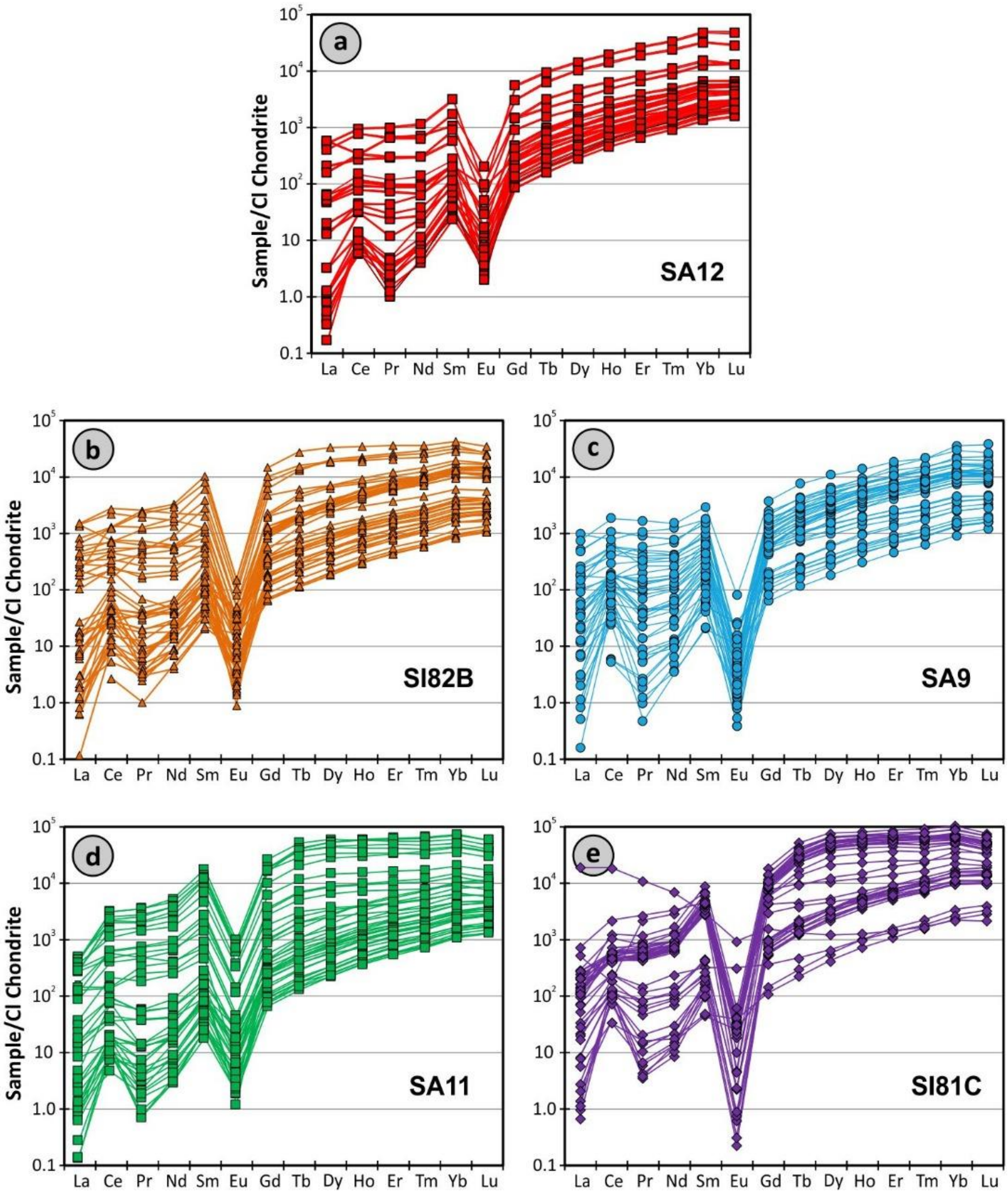
a
SA12
b
SI82B
c
SA9
d
SA11
e
SI81C
Sample/CI Chondrite
La Ce Pr Nd Sm Eu Gd Tb Dy Ho Er Tm Yb Lu

Figure 7

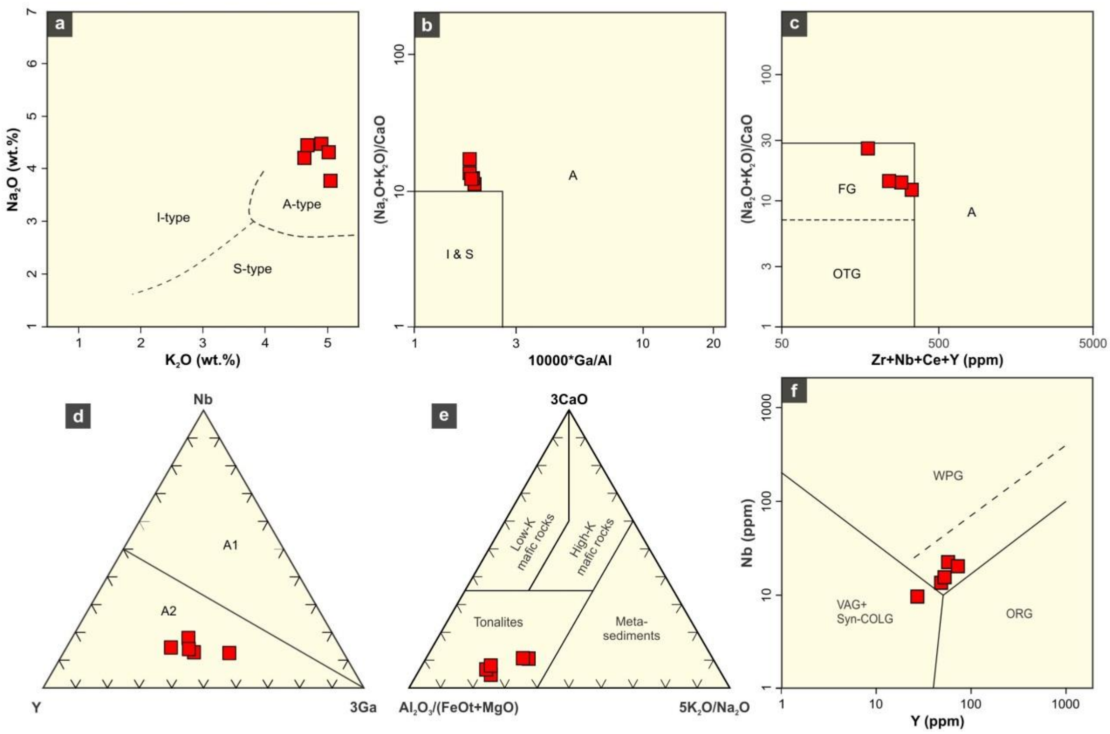

a
I-type
A-type
S-type
Na_2O (wt.%)
K_2O (wt.%)
b
A
I & S
$(Na_2O+K_2O)/CaO$
10000*Ga/Al
c
FG
A
OTG
$(Na_2O+K_2O)/CaO$
Zr+Nb+Ce+Y (ppm)
d
Nb
A1
A2
Y
3Ga
e
3CaO
Low-K mafic rocks
High-K mafic rocks
Tonalites
Meta-sediments
$Al_2O_3/(FeOt+MgO)$
$5K_2O/Na_2O$
f
WPG
VAG+ Syn-COLG
ORG
Nb (ppm)
Y (ppm)

Figure. 8

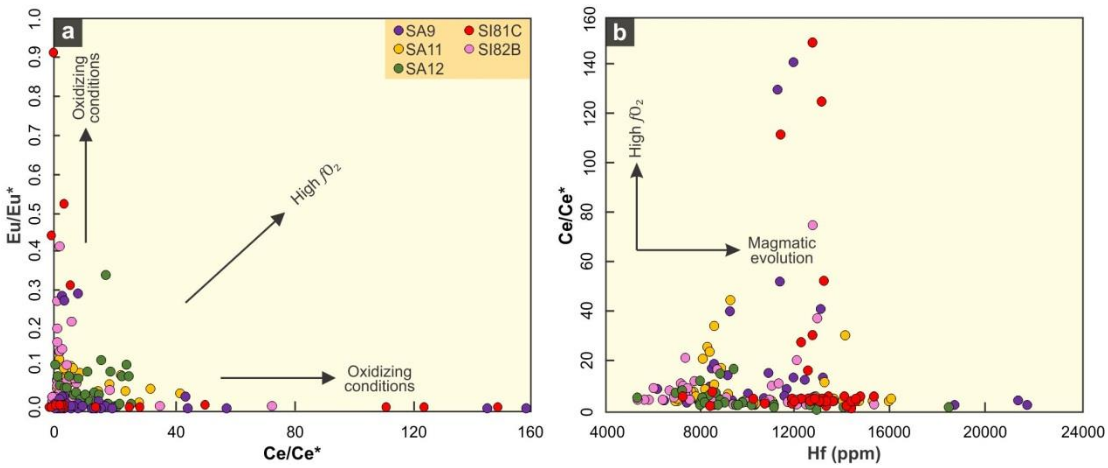

a
SA9
SI81C
SA11
SI82B
SA12
Oxidizing conditions
High fO_2
Oxidizing conditions
Eu/Eu*
Ce/Ce*
b
High fO_2
Magmatic evolution
Ce/Ce*
Hf (ppm)

Figure 9

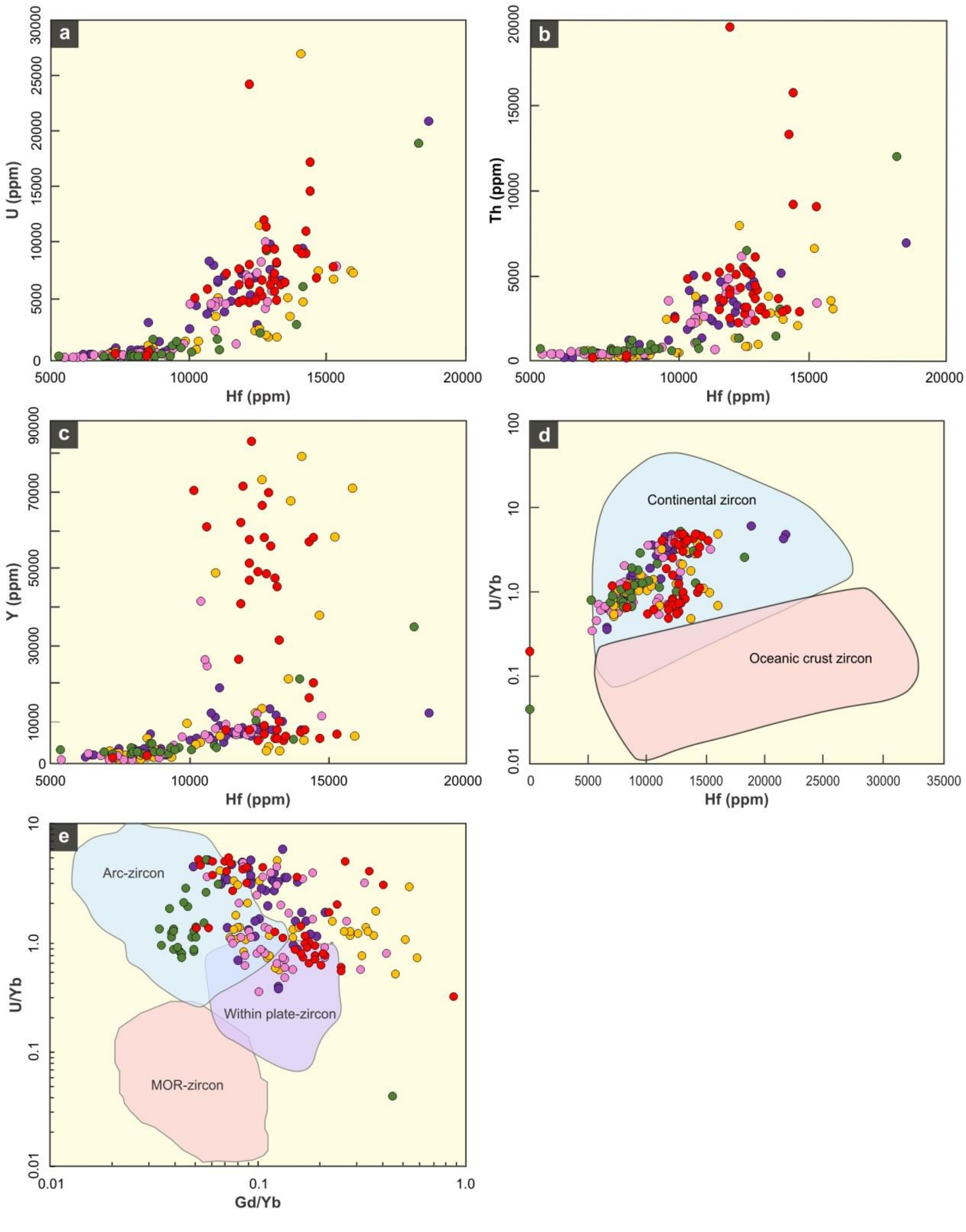
a
U (ppm)
Hf (ppm)
b
Th (ppm)
Hf (ppm)
c
Y (ppm)
Hf (ppm)
d
Continental zircon
Oceanic crust zircon
U/Yb
Hf (ppm)
e
Arc-zircon
Within plate-zircon
MOR-zircon
U/Yb
Gd/Yb

Figure 10

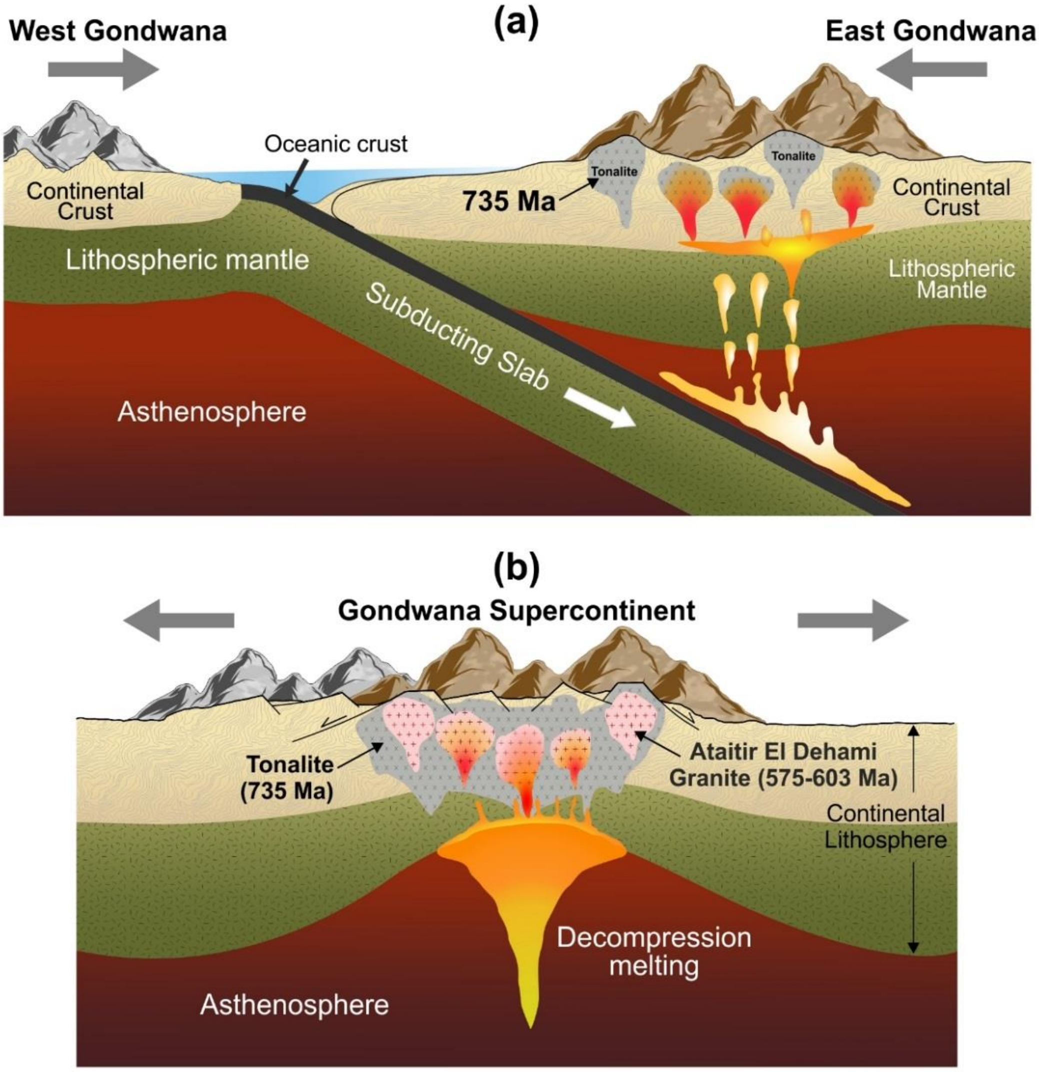
(a)
West Gondwana
East Gondwana
Oceanic crust
Continental Crust
Tonalite
Tonalite
735 Ma
Continental Crust
Lithospheric mantle
Lithospheric Mantle
Subducting Slab
Asthenosphere
(b)
Gondwana Supercontinent
Tonalite (735 Ma)
Ataitir El Dehami Granite (575-603 Ma)
Continental Lithosphere
Decompression melting
Asthenosphere

Click here to access/download
supplemental material (zip file)
Supplementary materials.rar